

Magnon polarons: Hybrid quasiparticles in coupled spin–lattice systems

Yufei Li(李宇飞) , Qi Gu(古琪) , Mingzhi Wang(王铭志) , Jia-Min Lai(来嘉敏) ,
Aizhuo Zhang(张爱茁) , Yameng Guo(郭雅萌) , Yuhao Xia(夏宇浩) , Yaowen Liu(刘要稳) ,
Jianwei Zhang(张建卫) , Wei Zhang(张伟) , Zhiyong Quan(全志勇) ,
Zhong Shi(时钟 , and Xiaohong Xu(许小红) ,
Citation: Chin. Phys. B, 2026, 35 (**4**): 047507. DOI: 10.1088/1674-1056/ae5efc
http://cpb.iphy.ac.cn; http://iopscience.iop.org/cpb

What follows is a list of articles you may be interested in

Creation and annihilation of artificial magnetic skyrmions with the electric field

Jun Cheng(程军), Liang Sun(孙亮), Yike Zhang(张一可), Tongzhou Ji(吉同舟), Rongxing Cao(曹荣幸), Bingfeng Miao(缪冰锋), Yonggang Zhao(赵永刚), and Haifeng Ding(丁海峰)
Chin. Phys. B, 2024, 33 (**3**): 037501. DOI: 10.1088/1674-1056/ad188f

Magnetocaloric properties and Griffiths phase of ferrimagnetic cobaltite $CaBaCo_4O_7$

Tina Raoufi, Jincheng He(何金城), Binbin Wang(王彬彬), Enke Liu(刘恩克), and Young Sun(孙阳)
Chin. Phys. B, 2023, 32 (**1**): 017504. DOI: 10.1088/1674-1056/ac8f39

Spin-phonon coupling in van der Waals antiferromagnet VOCl

Wen-Jun Wang(王文君), Xi-Tong Xu(许锡童), Jie Shen(沈洁), Zhe Wang(王哲), Shi-Le Zhang(张仕乐), and Zhe Qu(屈哲)
Chin. Phys. B, 2021, 30 (**10**): 107502. DOI: 10.1088/1674-1056/ac041f

Magnetoelastic coupling effect of $Fe_{10}Co_{90}$ films grown on different flexible substrates

Jiapeng Zhao(赵佳鹏), Qinhuang Guo(郭勤皇), Huizhong Yin(尹慧中), Jintang Zou(邹锦堂), Zhenjie Zhao(赵振杰), Wenjuan Cheng(程文娟), Dongmei Jiang(蒋冬梅), and Qingfeng Zhan(詹清峰)
Chin. Phys. B, 2020, 29 (**11**): 117501. DOI: 10.1088/1674-1056/abb22d

Magnetocaloric effect and critical behavior of the Mn-rich itinerant material Mn_3GaC with enhanced ferromagnetic interaction

Pengfei Liu(刘鹏飞), Jie Peng(彭杰), Mianqi Xue(薛面起), Bosen Wang(王铂森)
Chin. Phys. B, 2020, 29 (**4**): 047503. DOI: 10.1088/1674-1056/ab7da1

TOPICAL REVIEW — Advanced magnonics

Magnon polarons: Hybrid quasiparticles in coupled spin–lattice systems

Yufei Li(李宇飞)[1,2,†], Qi Gu(古琪)[1,†], Mingzhi Wang(王铭志)[2], Jia-Min Lai(来嘉敏)[1], Aizhuo Zhang(张爱茁)[1], Yameng Guo(郭雅萌)[1], Yuhao Xia(夏宇浩)[2], Yaowen Liu(刘要稳)[2], Jianwei Zhang(张建卫)[2], Wei Zhang(张伟)[1], Zhiyong Quan(全志勇)[1,‡], Zhong Shi(时钟)[2,§], and Xiaohong Xu(许小红)[1,¶]

[1] *Key Laboratory of Magnetic Molecules and Magnetic Information Materials of Ministry of Education & School of Materials Science and Engineering of Shanxi Normal University, Taiyuan* 030006, *China*

[2] *School of Physics Science and Engineering, Tongji University, Shanghai* 200092, *China*

(Received 21 December 2025; revised manuscript received 8 April 2026; accepted manuscript online 14 April 2026)

The concept of hybrid quasiparticles has emerged as a cornerstone of modern condensed matter physics, offering powerful means to control material properties and engineer new functionalities. Among these, the magnon polarons (MPs), a mixed state arising from the strong coupling between magnons (spin wave excitations) and phonons (lattice vibrations), have recently garnered significant attention. This review article comprehensively investigates recent advancements in the field of MPs. We begin by elucidating the fundamental magnetoelastic coupling mechanisms that underlie the formation of MPs. A detailed account of the primary experimental techniques, including inelastic neutron scattering and light scattering, are provided, highlighting their unique roles in probing the spectral and spatial properties of MPs. Furthermore, we explore the profound implications of the formation of MPs on spin and heat transport phenomena, such as the spin pumping, spin Seebeck effect, and spin Peltier effect. We then present a panorama of material systems where MPs have been experimentally observed, ranging from rare-earth iron garnets to antiferromagnets, multiferroic materials, and van der Waals magnets. Finally, we discuss emerging devices, applications and future research directions, underscoring the potential of MPs as integral components in next-generation spintronic and quantum information devices.

Keywords: magnon polarons, hybrid quasiparticles, magnetoelastic coupling, spin Seebeck effect

PACS: 75.30.Ds, 73.20.Mf, 71.38.–k, 67.30.hj

DOI: 10.1088/1674-1056/ae5efc **CSTR:** 32038.14.CPB.ae5efc

1. Introduction

To develop advanced technologies for information processing and energy conversion, it is essential to manipulate elementary excitations in solids, such as electrons, photons, magnons, and phonons. While these excitations were historically studied within separate theoretical frameworks, increasing attention has been devoted to their mutual interactions, which can generate hybrid quasiparticles with emergent properties beyond those of their individual constituents. Exploring such hybridization has become a central theme in modern condensed-matter physics, both for uncovering new physical phenomena and for enabling novel functionalities in quantum, spintronic, and energy-related devices.

Among these excitations, magnons and phonons are two fundamental bosonic quasiparticles in magnetic solids,[1,2] corresponding to collective excitations of the spin system and the crystal lattice, respectively. Spin waves arise from the collective precession of magnetic moments in magnetically ordered materials, and magnons are their quantized elementary excitations.[1,3–7] Owing to their chargeless nature, ability to carry angular momentum, and potentially low dissipation, magnons are regarded as promising information carriers for beyond-CMOS computing and coherent signal processing.[8–24] Phonons, on the other hand, are the quanta of lattice vibrations and govern the thermal and elastic properties of solids.[25] The dynamics of magnons and phonons are characterized by distinct dispersion relations, determined mainly by exchange and dipolar interactions in the former case, and by lattice symmetry and elastic constants in the latter.[4,26,27]

When magnon and phonon branches approach each other in energy–momentum space, magnetoelastic coupling (MEC) can hybridize the two modes and produce new mixed eigenstates with both spin and lattice character, namely magnon polarons.[28–37] Their formation is typically manifested through anticrossing behavior in the dispersion relation. Importantly, near these touching or anticrossing condi-

[†]These authors contributed equally to this work.

[‡]Corresponding author. E-mail: quanzy@sxnu.edu.cn

[§]Corresponding author. E-mail: shizhong@tongji.edu.cn

[¶]Corresponding author. E-mail: xuxh@sxnu.edu.cn

© 2026 Chinese Physical Society and IOP Publishing Ltd. All rights, including for text and data mining, AI training, and similar technologies, are reserved.

tions, the hybridization can make the observable consequences of MEC particularly pronounced, leading to enhanced spectroscopic intensity, modified quasiparticle lifetimes, and resonant anomalies in spin-caloritronic transport.[34,38,39] Because the MEC in magnetic solids stems from spin–orbit, dipole–dipole, and exchange interactions,[32–34,40] magnon polarons also provide an ideal platform for investigating quasiparticle hybridization, spin–lattice energy exchange, and dissipation in coupled bosonic systems. From an applied perspective, they offer new opportunities for manipulating spin, heat, and lattice degrees of freedom in magnonic, spintronic, and thermoelectric devices.[41] In this review, we summarize recent experimental progress on magnon polarons, with emphasis on their physical principles, detection methods, material platforms, and emerging functionalities.

From a theoretical point of view, the magnon, phonon, and coupled magnon-phonon subsystems can be described within a standard second-quantized framework. For compactness, we adopt below the standard second-quantized description of the coupled magnon-phonon system. According to previous theoretical works,[34,37,42] the magnon Hamiltonian can be written as

$$H_{\rm mag} = \sum_{\boldsymbol{k}} A_{\boldsymbol{k}} a^{\dagger}_{\boldsymbol{k}} a_{\boldsymbol{k}} + \left(\frac{B_{\boldsymbol{k}}}{2}\right)(a^{\dagger}_{\boldsymbol{k}} a^{\dagger}_{-\boldsymbol{k}} + a_{-\boldsymbol{k}} a_{\boldsymbol{k}}), \tag{1}$$

where $a^{\dagger}_{\boldsymbol{k}}$ ($a_{\boldsymbol{k}}$) are the magnon creation (annihilation) operators. The magnon dispersion is then given by $\hbar\omega_{\boldsymbol{k}} = \sqrt{A^2_{\boldsymbol{k}} - |B_{\boldsymbol{k}}|^2}$, and, in a commonly used form, can be expressed as

$$\omega_{\boldsymbol{k}} = \sqrt{D_{\rm ex}k^2 + \gamma\mu_0 H}\sqrt{D_{\rm ex}k^2 + \gamma\mu_0 H + \gamma\mu_0 M_{\rm s}\sin^2\theta_{\boldsymbol{k}}}, \tag{2}$$

where $D_{\rm ex}$, γ, μ_0, $M_{\rm s}$, and $\theta_{\boldsymbol{k}}$ denote the exchange stiffness, gyromagnetic ratio, vacuum permeability, saturation magnetization, and the angle between wave vector $\boldsymbol{k}$ and the magnetic field $\boldsymbol{H}$, respectively.[43–45]

Phonons represent the collective oscillatory motion of atoms around their equilibrium positions.[25] They are central to the thermal and elastic response of solids. For an isotropic elastic medium, the acoustic phonon Hamiltonian can be written as[34,37,46]

$$H_{\rm ph} = \sum_{\boldsymbol{k},\lambda} \hbar\omega_{\lambda\boldsymbol{k}}\left(c^{\dagger}_{\lambda\boldsymbol{k}} c_{\lambda\boldsymbol{k}} + \frac{1}{2}\right), \tag{3}$$

where $c^{\dagger}_{\lambda\boldsymbol{k}}$ ($c_{\lambda\boldsymbol{k}}$) are the phonon creation (annihilation) operators for branch λ. The corresponding acoustic phonon dispersion is[37]

$$\omega_{\lambda\boldsymbol{k}} = c_{\lambda}\,|\boldsymbol{k}| \tag{4}$$

with c_{λ} being the sound velocity of the corresponding phonon branch.

The interaction between the spin and lattice subsystems is provided by MEC. As first discussed by Kittel,[27,46] this coupling can mix magnetic and elastic excitations when their uncoupled dispersions approach one another. A representative MEC Hamiltonian under linear approximation can be written as[34,35,37,47–49]

$$\begin{aligned} H_{\rm mec} = {} & \hbar n B_{\perp}\left(\frac{\gamma\hbar^2}{4M_{\rm s}\rho}\right)^{1/2} \sum_{\boldsymbol{k},\lambda} k\omega^{-\frac{1}{2}}_{\boldsymbol{k}\lambda}\, {\rm e}^{-{\rm i}\phi} a_{\boldsymbol{k}}(c_{\lambda-\boldsymbol{k}} + c^{\dagger}_{\lambda\boldsymbol{k}}) \\ & \times (-{\rm i}\delta_{\lambda 1}\cos 2\theta_{\boldsymbol{k}} + {\rm i}\delta_{\lambda 2}\cos\theta_{\boldsymbol{k}} - \delta_{\lambda 3}\sin 2\theta_{\boldsymbol{k}}) \\ & + {\rm H.c.}, \end{aligned} \tag{5}$$

where $B_{\perp}$ is the magnetoelastic coupling constant, $n = 1/a_0^3$ is the number density of spins with lattice constant a_0, ρ is the average mass density. $\boldsymbol{k} = k(\sin\theta\cos\phi, \sin\theta\sin\phi\cos\theta)$ is the wave vector in spherical coordinates, and $\delta_{\lambda i}$ is the Kronecker delta. The total Hamiltonian for the coupled system is then approximated as[35,37,42,49]

$$H = H_{\rm mag} + H_{\rm ph} + H_{\rm mec}. \tag{6}$$

Diagonalizing this Hamiltonian yields the hybridized eigenmodes of the coupled spin–lattice system. When a magnon branch and a phonon branch approach each other in both frequency and wave vector, MEC causes them to hybridize and form new mixed quasiparticles, namely magnon polarons. These modes are no longer purely magnetic or purely elastic, but coherent superpositions of both. Their most characteristic signature is an anticrossing in the dispersion relation, accompanied by a redistribution of magnonic and phononic spectral weight.[35–37,42,50]

Magnon–phonon coupling is therefore not merely a small perturbation, but can substantially modify the dynamics and transport properties of both the spin and lattice subsystems. The ability to engineer and control this coupling has become an important theme in modern condensed-matter physics, opening opportunities for efficient interconversion among spin, lattice, heat, and charge degrees of freedom. A wide range of experiments, including inelastic neutron scattering (INS),[39,51,52] light scattering (Brillouin light scattering (BLS) and Raman spectroscopy),[53–65] spin pumping,[66] spin Seebeck effect (SSE),[35–38,42,50,67–75] and the spin Peltier effect (SPE),[76] have revealed the rich physics of magnon polarons. Moreover, because magnon and phonon dispersions vary significantly among different materials, the resulting hybridization phenomena are highly tunable and provide a foundation for designing magnon-polaron-based functionalities and devices. This review aims to summarize recent experimental progress on magnon polarons, with an emphasis on their physical principles, experimental probes, material platforms, and potential applications, as outlined in Fig. 1.

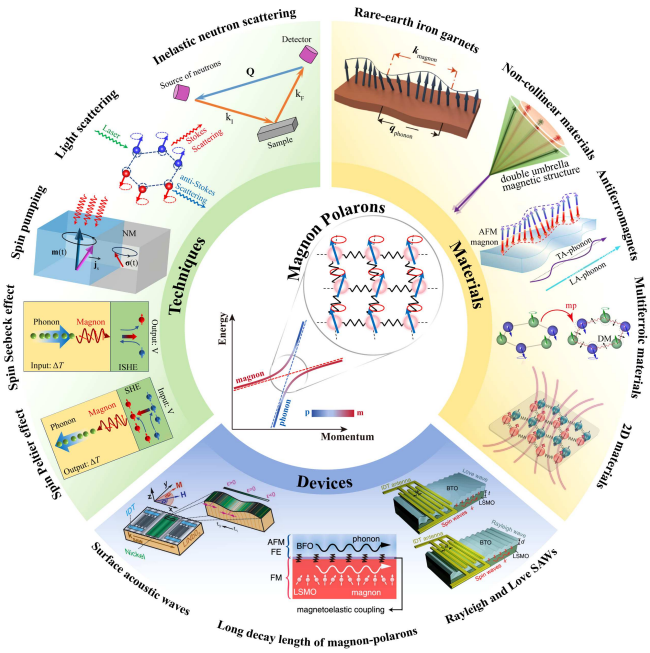


Fig. 1. Schematic overview of experimental techniques, materials, and devices for magnon polarons. Reprinted with permission from Refs. [50,52,57,69,77–79]. Copyright 2021 by American Physical Society. Copyright 2020 by American Physical Society. Copyright 2023 by Springer Nature. Copyright 2021 by American Physical Society. Copyright 2011 by American Physical Society. Copyright 2021 by Springer Nature. Copyright 2023 by American Physical Society.

2. Observation techniques and detection methods for magnon polarons

2.1. Direct observation of magnon (polarization) polarons by inelastic (polarized) neutron scattering

The precessional direction of magnons relative to the external magnetic field ($\boldsymbol{H}$) can be counterclockwise or clockwise, which respectively determines the existence of right-handed (α mode, positive polarization) or left-handed (β mode, negative polarization) magnon chiralities. As shown in Fig. 2(a), the magnetization $\boldsymbol{m}$ precesses only counterclockwise in ferromagnets (FMs) as a result of the negative gyromagnetic ratio (γ) of electronic spin, thereby the magnon chirality is locked in the α mode.[80] Both α and β modes with opposite polarizations exist in antiferromagnets (AFMs) in the THz frequency regime,[18,81–93] but they are degenerate unless large $\boldsymbol{H}$ is applied. The ferrimagnets (FiMs) possess two antiparallel magnetic sublattices and support two separated magnon modes with opposite polarizations as well due to the intersublattice exchange field.[94–101] As one of well-known FiMs, yttrium iron garnet ($Y_3Fe_5O_{12}$, YIG) possesses an extremely low Gilbert damping factor,[45,102,103] long magnon-propagation length,[5,104,105] and high Curie temperature ($\sim$ 560 K),[106] making it an essential material for research in spintronics, spin caloritronics and magnonics.[102] YIG exhibits a complex cubic crystal structure, as shown in Fig. 2(b). The Y^{3+} ions reside in c-sites (dodecahedral) and are nonmagnetic. The magnetic properties of YIG are exclusively determined by the Fe^{3+} ions, whose magnetic moments on the a-site (octahedral) and d-site (tetrahedral) sublattices are coupled antiparallel via strong superexchange interactions through the intervening oxygen ions.[107,108] Since the number of Fe^{3+} ions differs between the a-site (3) and d-site (2) sublattices, their magnetic moments fail to cancel each other completely, thereby generating a net magnetic moment with a theoretical saturation magnetization of approximately 5 μ_B per formula unit.[107] By using polarized neutron scattering (Fig. 2(c)), both the negative and the positive polarization of magnon modes were directly measured (Fig. 2(d)),[109] confirming that YIG must be a ferrimagnet and possess a rich spectrum of spin-wave modes beyond a simple parabolic dispersion.[110] The gap between those two magnon modes in YIG is caused by the exchange field between the a-site and d-site sublattices. Magnon modes are thermally occupied below k_BT. The gap of a negative polarized magnon mode is comparable to the thermal energy k_BT at 300 K, just as indicated by the blue dashed line representing k_BT in Fig. 2(d).

INS is a pivotal spectroscopic technique that yields the first direct verification of magnetic excitations such as magnons,[6] and allows for the detailed measurement of their coupling with phonons.[52] When a neutron (uncharged but with spin 1/2) scatters inelastically from a magnetic material, it can create or annihilate a magnon, thereby losing or gaining an amount of energy ($\hbar\omega$) and momentum ($\hbar q$) equal to that of the magnon. By detecting the energy and momentum transfer of the scattered neutrons, INS directly maps out the full magnon dispersion relations $E(q)$ across the entire Brillouin zone (see Subsection 3.4). When investigating magnon–phonon coupling, INS is a premier technique due to its unique ability to simultaneously probe both the energy and momentum of magnetic and lattice excitations. The most direct evidence is an anti-crossing or repulsion in the dispersion relations observed in the energy–momentum maps, where the magnon and phonon branches hybridize instead of crossing, which indicates the formation of MPs.[52] INS also reveals coupling through the transfer of spectral weight between the magnon and phonon modes and a broadening of the excitation linewidths at the interaction region due to the reduced lifetime of the original excitations.[51] Using INS to probe spin waves and transverse acoustic (TA) and longitudinal acoustic (LA) phonons of YIG at different positions of reciprocal space (Fig. 2(e)), Man *et al.* found that, compared to 9.1 T, hybridized magnon–polaron scattering at the intersecting points has a larger intensity at 0 T and magnons remain unchanged at other wave vectors (Fig. 2(f)).[51] Magnon–phonon coupling in YIG enhances the hybridized scattering intensity. This is different from splitting and opening up gaps at the magnon and acoustic phonon dispersion intersecting points.

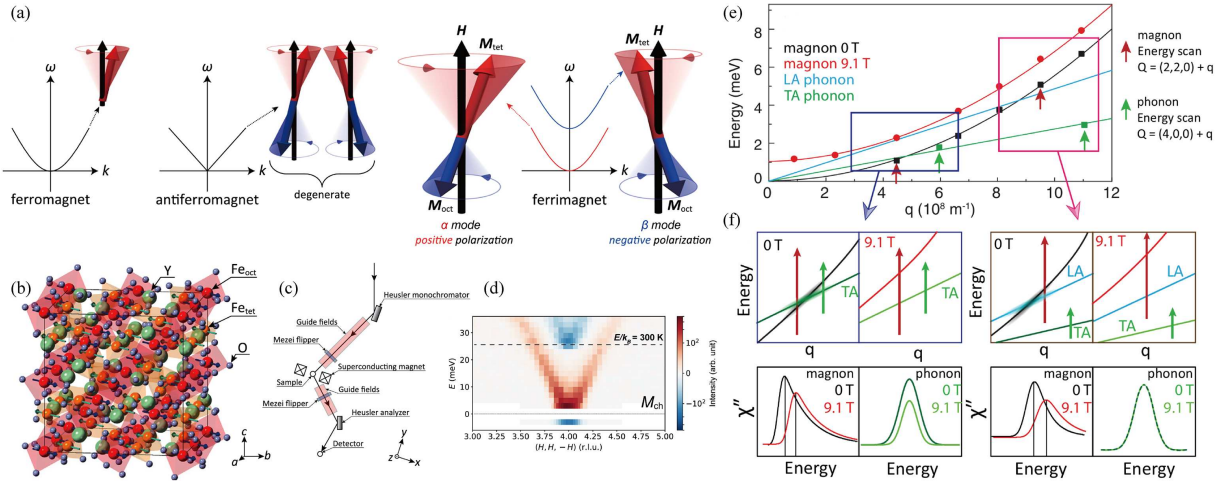


Fig. 2. (a) Illustration of polarization for magnon modes in FM, AFM and FiM. (b) Crystallographic unit cell of YIG. (c) Sketch of polarized neutron scattering instrument with bold black arrows denoting the neutron path. (d) Magnon spectra of YIG at RT measured with inelastic polarized neutron scattering. Reprinted with permission from Ref. [109]. Copyright 2020 by American Physical Society. (e) Magnon and phonon dispersions of YIG at 100 K under 0 and 9.1 T. The blue and pink squares indicate magnon–phonon crossing parts and are expanded to (f), where the bottom panels summarize the magnetic field effect on spin waves, hybridized excitations, and TA phonons.[51] Here, the phonon velocity $C_{\mathrm{T}} = 3.9$ km/s for TA branch and $C_{\mathrm{L}} = 7.2$ km/s for LA branch.[35] Reprinted with permission from Ref. [51]. Copyright 2017 by American Physical Society.

2.2. Detection of magnon polarons via light scattering

Light scattering refers to the phenomenon where the direction of light propagation is deflected when it interacts with inhomogeneities inside the medium. These inhomogeneities include particle number density, charge density, spin density, etc. Scattering processes that occur without changes in photon frequency are termed elastic scattering, whereas those involving a frequency shift are known as inelastic scattering.[56,111,112] The inelastic scattering process satisfies the law of energy and momentum conservation by annihilating or generating quasiparticles such as phonons and magnons, which can be expressed as $\hbar\omega_{\mathrm{S(aS)}} = \hbar\omega_{\mathrm{i}} \mp \hbar\Omega$ and $\hbar\boldsymbol{k}_{\mathrm{S(aS)}} = \hbar\boldsymbol{k}_{\mathrm{i}} \mp \hbar\boldsymbol{q}$, respectively, as shown in Figs. 3(a) and 3(b). ω_i, Ω, and $\omega_{\mathrm{S(aS)}}$ are the frequency of the incident photons, quasiparticles, and Stokes (or anti-Stokes) scattering photons, respectively. $\boldsymbol{k}_{\mathrm{i}}$, $\boldsymbol{q}$, and $\boldsymbol{k}_{\mathrm{S(aS)}}$ are the wavevector of the incident photons, quasiparticles, and Stokes (or anti-Stokes) scattering photons, respectively. Therefore, scattering spectroscopy provides an effective technique to probe these quasiparticles and hybridization among them. Modern Raman instruments are equipped with a combination of filters and fine gratings, which can detect quasi-particles with a frequency larger than 150 GHz (about 5 cm^{-1}). While Brillouin instruments utilizing a multi-pass tandem Fabry–Pérot interferometer can detect quasi-particles with a frequency from 500 MHz to 1.5 THz.[113] Hence, as shown in Fig. 3(c), Raman spectroscopy is commonly used to probe optical phonons and relatively fewer high-frequency magnons, while Brillouin spectroscopy is employed to study acoustic phonons as well as most magnons.[59,62] Magnon–phonon hybridization under strong magnon–phonon coupling, anti-crossing features typically emerge in the energy dispersion, which can be directly observed through $\boldsymbol{H}$-dependent Raman or Brillouin spectroscopy.[53–55,57,58,60,64,114–116] The light scattering technique provides a robust approach to investigating MPs.

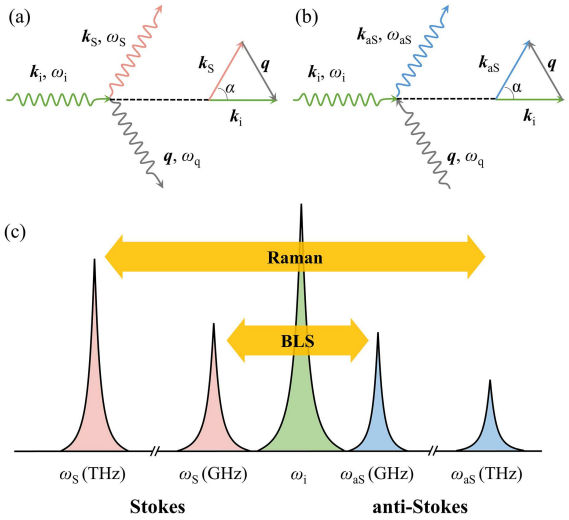


Fig. 3. The schematic diagram and spectra of inelastic light scattering. Schematic diagrams of (a) the Stokes scattering, (b) the anti-Stokes scattering. (c) The spectra of Raman scattering and Brillouin scattering.

2.3. Probing magnon polarons via the spin pumping

Spin pumping refers to a phenomenon that converts magnetization precession into a pure spin current.In YIG/Pt heterostructures, when the magnetization in YIG precesses coherently under an in-plane external $\boldsymbol{H}$ and microwave magnetic field $\boldsymbol{h}$ (Fig. 4(a)), it pumps a magnon current carrying spin angular momentum across YIG/Pt interface into Pt layer. The spin current can then be detected electrically via the inverse spin Hall effect (ISHE), which converts it into a measurable voltage V_{ISHE} (Fig. 4(a)). Hayashi *et al.* reported that, compared to microwave power $P = 50$ mW, an additional anomalous signal of P_{abs} and V_{ISHE} induced by the parametrically excited magnons shows up around 40–100 mT for $P = 250$ mW

(Fig. 4(b)), which involves the splitting of microwave photons from the pumping microwave into pairs of magnons with pumping frequency $f_p/2$ and opposite wave vectors $\boldsymbol{k} \neq 0$ through the virtual excitation of the uniform magnons with f_p (Fig. 4(c)).[66,124] The wave vector of the parametric magnons can be tuned by shifting the magnon dispersion in the k–f space using $\boldsymbol{H}$, the dispersions of magnons and TA phonons, as shown in Fig. 4(d).[66] At low $\boldsymbol{H}$ ($\sim$ 40 mT), because the dipole-exchange magnons are unavailable at $f_p/2$ (f_p = 6.5 GHz), only exchange magnons with $k \sim 10^5$ cm^{-1} can be excited, thereby no anomaly will occur in the spin-pumping efficiency ($\kappa = V_{ISHE}/P_{abs}$). By increasing $\boldsymbol{H}$, the magnon dispersion shifts to lower k and higher f in k–f space, and dipole-exchange magnons with $k \sim 10^3$–10^4 cm^{-1} can be excited in the proximity of the intersection of the uncoupled magnon and phonon dispersions at approximately 78 mT, resulting in the peak of the normalized spin-pumping efficiency $\bar{\kappa}$–$\boldsymbol{H}$ curves associated with magnon–phonon coupling and forming MPs (Fig. 4(e)),[66] where $\bar{\kappa} \equiv \kappa(\mu_0 H)/\kappa$ ($\mu_0 H$ = 60 mT) at different f_p.

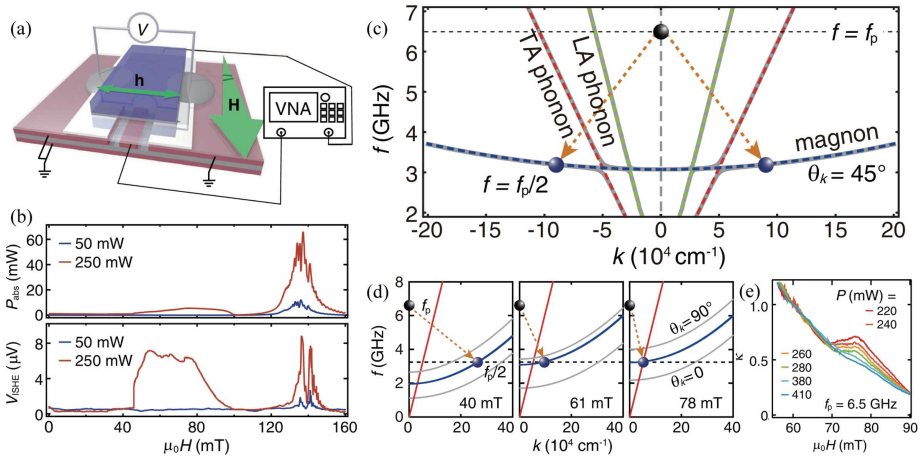


Fig. 4. (a) A schematic illustration of the spin pumping setup. (b) $\boldsymbol{H}$ dependence of the microwave absorption intensity P_{abs} and the microwave parametric pumping V_{ISHE} for the microwave power at 50 mW and 250 mW. (c) A schematic of the microwave paramagnetic pumping. The dispersions of magnons, TA and LA phonons in a YIG film with anticrossings due to the magnon–phonon coupling, where f and k are the frequency and wave number. The magnon dispersion was calculated for the angle $\theta_k = 45°$ between $\boldsymbol{k}$ and $\boldsymbol{H}$. A uniform-mode magnon with frequency of f_p at $\boldsymbol{k} = 0$ is excited virtually and splits into a pair of magnons with frequency of $f_p/2$ at opposite $\boldsymbol{k} \neq 0$. (d) The dispersions of magnons and TA phonons at different $\boldsymbol{H}$. (e) $\boldsymbol{H}$ dependence of $\bar{\kappa}$ at f_p = 6.5 GHz with various microwave powers. Reprinted with permission from Ref. [66]. Copyright 2018 by American Physical Society.

2.4. Probing magnon polarons via the spin Seebeck effect and spin Peltier effect

The SSE describes the generation of a spin current driven by a temperature gradient (∇T) in magnetic materials, encompassing FMs,[125,126] FiMs,[127,128] AFMs,[129–131] 2D materials,[14,132–135] paramagnets[136,137] and altermagnets,[138–141] which can be electrically detected through the ISHE in an adjacent metallic layer. Owing to its capability of enabling the interconversion among heat flow, spin current, and charge current, the SSE demonstrates promising applications in waste heat recovery devices and spin thermoelectric sensors.[142] The SSE was first discovered in the permalloy/Pt system using transverse configuration, in which a ∇T is applied parallel to the film plane.[125] Then, the longitudinal SSE (LSSE) was observed in YIG/Pt heterostructure.[127,128] In the LSSE configuration (Fig. 5(a)), a ∇T is applied across the YIG/Pt interface and generates a magnon current along ∇T in YIG (Fig. 5(b)), which induces spin accumulation at the interface of YIG/Pt and becomes a conduction-electron spin current. Finally, the spin current generated in the YIG layer is converted into a measurable voltage via the ISHE in the adjacent heavy metal Pt layer (also in W, Ta), allowing detection of the spin signal (Fig. 5(c)). The nonlocal SSE (nlSSE) geometry was also developed (Fig. 5(d)), which consists of spin injection and detection.[105] By varying the distance between injection and detection contacts, the transport properties of spin carriers in the channel can be accurately determined.

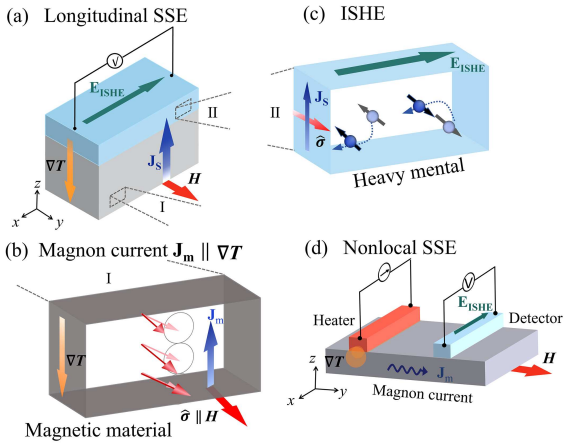


Fig. 5. Schematic illustrations of the (a) longitudinal SSE, (b) magnon current J_m, (c) ISHE, and (d) nonlocal SSE.

The LSSE and nlSSE are usually used in magnetic insulator systems, where heat current generates magnon current without charge movement. This facilitates the development of energy-efficient magnonic devices based on the SSE, for example magnon valves,[11,12] magnon switches,[21,143]

magnon filters,[100] and magnon transistors,[14] offering significant potential for low-power, high-integration magnonic applications. Furthermore, the SSE can serve as a sensitive probe into the fundamental properties of magnetic materials, such as magnetic order,[75,82,133] spin correlation,[131,136] magnon polarization[75,82,100,144–147] and magnon–phonon hybridization.[35–38,42,50,68–73]

MPs were detected both in $\boldsymbol{H}$-dependent LSSE[35] and nlSSE[36] in the YIG/Pt bilayers (Figs. 6(a)–6(c)). During a fine $\boldsymbol{H}$ scan, the SSE anomalies manifest as small sharp peak/dip structures, which occur at ~ 2.6 T and ~ 9.3 T as indicated by the blue and green triangles. The underlying physics requires analyzing the dispersion relations of magnons and phonons in YIG (Fig. 6(d)). The dispersion of magnons in YIG takes the form of a parabolic curve and can be modified by the $\boldsymbol{H}$,[35,37,43,45,50] according to formula (2) in the Introduction part. In contrast, the dispersion curves of TA and LA phonons cannot be modified by $\boldsymbol{H}$ and in the relevant regime can be expressed as $\omega = kc_{\mathrm{T(L)}}$, where c_{T} and c_{L} are the sound velocities of the TA and LA phonons, respectively. At low $\boldsymbol{H}$ (@1 T in Fig. 6(d)), magnon and TA phonon dispersion curves intersect with each other twice. Anticrossings are observed between magnon and TA phonon branches at lower (inset i in Fig. 6(d)) and higher (inset ii in Fig. 6(d)) frequencies, accompanied by the formation of MPs.[35,67] As the $\boldsymbol{H}$ increases, the magnon branch exhibits an upward shift toward high frequencies due to Zeeman interaction, while the phonon branch remains unchanged. When the $\boldsymbol{H}$ reaches the critical fields $\boldsymbol{H}_{\mathrm{TA}}$ and $\boldsymbol{H}_{\mathrm{LA}}$, the magnon branch is tangent to the TA- and LA-phonon branches (inset iii in Fig. 6(d)). The $\boldsymbol{H}_{\mathrm{TA(LA)}}$ can be expressed as $\mu H_{\mathrm{TA(LA)}} = c^2_{\mathrm{T(L)}}/4\gamma D_{\mathrm{ex}}$. Under these "touching" conditions, the magnon and phonon branches undergo coupling across the broadest volumetric range within momentum space with respect to the anticrossing situation, thereby yielding the most pronounced effect with respect to the magnon-polaron formation process. Note that the MP anomalies in LSSE appear as peaks, while those in nlSSE appear as dips (Fig. 6(c)). Flebus *et al.* developed Boltzmann transport theory and reported that the peaks or dips in SSE anomalies are related to the ratio between magnetic and non-magnetic impurity-scattering potentials,[37] $\eta = \tau^{-1}_{\mathrm{mag}}/\tau^{-1}_{\mathrm{ph}}$, where τ^{-1}_{mag} and τ^{-1}_{ph} are the scattering rates of magnons and phonons, respectively. For $\eta > 1$ (< 1), or more precisely, when the scattering rate of magnons τ^{-1}_{mag} is larger (smaller) than that of phonons τ^{-1}_{ph}, MPs may have a longer (shorter) relaxation time than pure magnons. The SSE anomalies are therefore peaks (dips) structure at the "touching" fields (Fig. 6(e)). For $\eta = 1$, the SSE anomalies have almost disappeared. Accordingly, it can be explained that the acoustic quality of YIG film in Fig. 6(b) is much better than the magnetic quality ($\eta > 1$), while the YIG grown by liquid phase epitaxy in Fig. 6(c) belongs to the low acoustic quality ($\eta < 1$). So far, magnon-polaron peaks have been detected in several magnetic films via LSSE experiments. Shi *et al.* reported that the magnon-polarons LSSE anomalies in YIG-bulk/Pt experienced a dip-to-peak transition as temperature increased (Fig. 6(f)), which is attributed to the rapidly rising four-magnon scattering rate at high temperature and leading to the transformation of $\eta < 1$ into $\eta > 1$ (Fig. 6(g)). This work explicitly demonstrates that magnon-magnon scattering plays a critical role in the magnon-polaron SSE, and thus provides valuable insights into the microscopic mechanism of magnon-polaron formation.

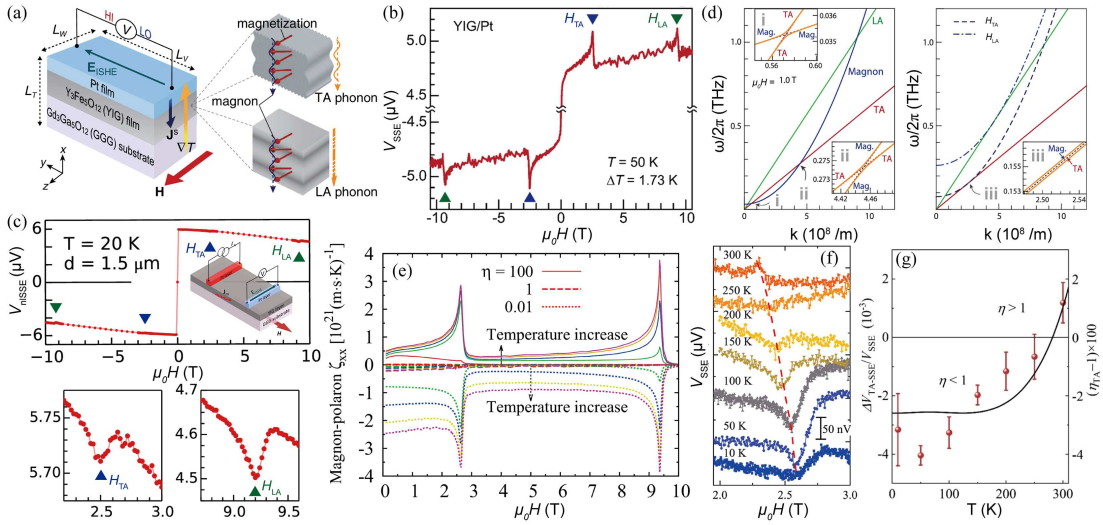


Fig. 6. MPs in SSE for YIG. (a) The LSSE in YIG/Pt sample. The right side illustrates the propagation of magnon and TA (LA) phonons. $\boldsymbol{H}$ dependence of the voltage of LSSE at 50 K (b) and nlSSE at 20 K (c). Reprinted with permission from Refs. [35,36]. Copyright 2016 by American Physical Society. Copyright 2017 by American Physical Society. The inset in (c) is nlSSE setup of YIG/Pt sample. The blue and green triangles indicate the $\boldsymbol{H}_{\mathrm{TA}}$ and $\boldsymbol{H}_{\mathrm{LA}}$ at SSE anomalies. (d) Magnon–phonon dispersion relations in YIG at 1 T, $\boldsymbol{H}_{\mathrm{TA}}$ and $\boldsymbol{H}_{\mathrm{LA}}$. The insets (i, ii and iii) show anticrossing and "touching" situations. Reprinted with permission from Ref. [67]. Copyright 2022 by Annual Reviews. (e) The $\boldsymbol{H}$ and T dependence of the SSC for different values of the ratio η between magnon and phonon impurity-scattering potentials. Reprinted with permission from Ref. [37]. Copyright 2017 by American Physical Society. (f) Evolution of LSSE anomalies near $\boldsymbol{H}_{\mathrm{TA}}$ with $\boldsymbol{H}$ and T. (g) Temperature dependencies of calculated $\eta_{\mathrm{TA}} - 1$ (solid line) and measured $\Delta V_{\mathrm{TA-SSE}}/V_{\mathrm{SSE}}$ (circles). Reprinted with permission from Ref. [50]. Copyright 2021 by American Physical Society.

As the Onsager reciprocal of the SSE, SPE refers to the phenomenon where heat current is generated via spin current,[148,149] which also represents a direct interconversion between spin information and heat energy, forming a cornerstone of spin caloritronics.[41] Therefore, similar magnon-polaron anomalies may also show up in the SPE. A recent experiment has investigated $\boldsymbol{H}$-dependent SPE utilizing a junction composed of Bi- and Ga-substituted lutetium iron garnet $Lu_2BiFe_4GaO_{12}$ (BiGa:LuIG) and Pt,[76] as shown in Fig. 7(a). When a square-wave charge current $\boldsymbol{J}_c$ of amplitude $\Delta\boldsymbol{J}_c$ is applied to the Pt layer (Fig. 7(b)), a spin current $\boldsymbol{J}_s$ is generated, which in turn creates a nonequilibrium spin accumulation $\boldsymbol{\mu}_s$ at the BiGa:LuIG/Pt interface. By the interfacial spin-exchange coupling, $\boldsymbol{\mu}_s$ induces scattering processes that create or annihilate nonequilibrium magnons: when $\boldsymbol{\mu}_s$ is parallel (antiparallel) to the equilibrium magnetization in BiGa:LuIG, the magnon population in BiGa:LuIG increases (decreases). This process is accompanied by a heat flow $\boldsymbol{J}_q$ between the BiGa:LuIG/Pt, which in turn modulates the system temperature. The heat current $\boldsymbol{J}_q$ induced by the SPE gives rise to a temperature difference between the Pt and BiGa:LuIG films in the vicinity of their interface — an effect detected by the E-type thermocouple (TC) affixed to the top of the Pt film using varnish and ultimately manifested as ΔV_{TC} (Fig. 7(b)). In the $\boldsymbol{H}$-dependent ΔV_{TC} curve, two anomalous peak structures appear for the fields H_{TA} (0.16 T) and H_{LA} (1.0 T) at which the magnon dispersion curve of BiGa:LuIG touches the TA-phonon and LA-phonon dispersion curves and forms MPs, as marked by the blue and red triangles in Fig. 7(c), respectively. The magnon-polaron anomalies observed in SPE are consistent with the previous SSE measurement, but they occur at a lower $\boldsymbol{H}$, which is attributed to the doping effect (see Fig. 8).

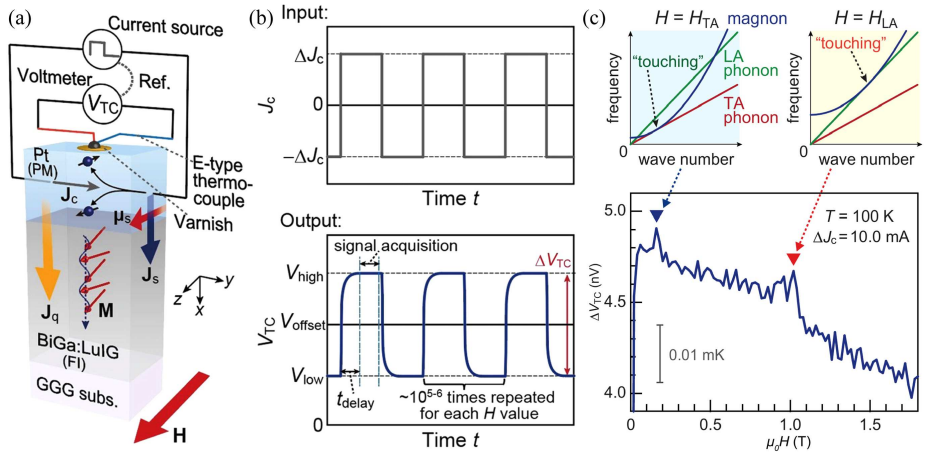


Fig. 7. (a) A schematic illustration of the SPE in BiGa:LuIG/Pt. (b) Input signal: A square-wave charge current J_c with amplitude ΔJ_c. Output signal: A TC voltage V_{TC} that responds to the change in the J_c polarity, ΔV_{TC} ($= V_{high} - V_{low}$). (c) $\boldsymbol{H}$-dependence of ΔV_{TC} at 100 K and $\Delta J_c = 10$ mA. The blue and red triangles denote the H_{TA} and H_{LA}, respectively, where the magnon, TA-phonon, and LA-phonon dispersion relations for BiGa:LuIG are shown in the upper plane. Reprinted with permission from Ref. [76]. Copyright 2020 by American Physical Society.

The experimental identification of MPs employs a suite of complementary techniques. The major characteristics of INS that make it ideal for these studies include its direct sensitivity to magnetic moments, its access to wide ranges of energy and momentum transfers relevant to collective excitations, and its ability to probe bulk single crystals. However, the main limitation of INS is the requirement for intense neutron sources (reactors or spallation sources) and often large single-crystal samples, making it a technique suited for large-scale facilities. Spectroscopic methods like INS and BLS are pivotal for directly mapping the dispersion relations, where the characteristic anti-crossing gap between magnon and phonon branches serves as definitive evidence. Raman spectroscopy can also probe higher-energy hybrid modes. Electrically, spin pumping directly injects a pure spin current into the magnetic system, which can efficiently excite MPs at the relevant interfaces (see Subsection 4.1). The key advantages of spin pumping lie in its direct sensitivity to the spin dynamics and its ability to probe these hybridized states with high resolution. The SSE is a vital and powerful tool for probing MPs for both bulk samples and thin films, primarily due to its unique sensitivity for spin currents, spin accumulation, and interfacial spin dynamics across magnetic heterostructures.[67] A simple applied thermal gradient excites a broad spectrum of magnons, and when these energies are tangent to phonon dispersions, the resulting magnon-polaron formation creates distinct resonant features (peaks/dips) in the SSE voltage. This provides a direct fingerprint for mapping MEC and dispersion relations. Furthermore, MPs can be detected by both local and nonlocal SSE, making it a distinctive method for understanding hybrid spin–lattice dynamics in magnetic materials. The SPE, as the reciprocal phenomenon, provides additional verification by detecting localized temperature changes induced by spin currents under the influence of magnon–phonon coupling. Together, these optical, electrical, and thermal approaches offer a comprehensive toolkit for unraveling the dynamics of MPs.

3. Material platforms for magnon polarons

3.1. Tuning magnon polarons via non-magnetic ion substitutions in YIG

Although MPs induced by magnon–phonon coupling have been observed in SSE within YIG, this effect always occurs under high $\boldsymbol{H}$ due to the intrinsic dispersions of magnon and phonon in YIG, and its magnitude is relatively small compared to the value of the SSE itself,[35,36,50] which narrows the breadth of practical applications. Given that magnon dispersion and phonon dispersion relations are pivotal to the magnon-polaron SSE, modifying these two dispersion relations naturally opens up feasible avenues for low-field manipulation and amplification of MPs. By engineering the magnon and phonon dispersions via substituting non-magnetic ions at the Y-sites or Fe-sites of YIG, it is possible to tune $\boldsymbol{H}$ at which the strength of magnon–phonon hybridization effects is maximized.

Bismuth (Bi) substituted Y-sites of YIG (Bi:YIG) is a key material in magnetics and magneto-optics,[150,151] as its substitution dramatically enhances the garnet's Faraday rotation angle compared to pristine YIG and also increases the magnetoelastic interaction, thereby providing a new opportunity for its applications in spintronics and magnonics. Furthermore, Kikkawa *et al.* reported that Bi:YIG shows a decrease in sound velocities for both TA and LA modes compared to YIG (Fig. 8(a)),[72] as a result of Bi having a much larger atomic mass (209) than Y (89). The decrease in sound velocities will reduce the magnon–phonon touching $\boldsymbol{H}$ and reduce touching ω (Fig. 8(b)). Therefore, the $Bi_xY_{3-x}IG$ films serve as a valuable platform for the systematic study of magnon-polaron anomalies in SSE. For $x = 0$, the peak at the lower (higher) H appears at $\boldsymbol{H}_{\rm TA} = 2.51$ T ($\boldsymbol{H}_{\rm LA} = 9.27$ T), which is consistent with previous studies.[35–37,50] By increasing the Bi amount x ($x = 0.5$ and 0.9), both the peak fields ($\boldsymbol{H}_{\rm TA} = 2.15$ T and 2.06 T, $\mu_0\boldsymbol{H}_{\rm LA} = 8.18$ T and 7.47 T) actually shift toward lower $\boldsymbol{H}$ values (Fig. 8(c)). The frequency value ω for the touching point between the magnon and TA (LA)-phonon branches at $\boldsymbol{H}_{\rm TA}$ ($\boldsymbol{H}_{\rm LA}$) reduces, as the sound velocities decrease with an increase in Bi amount x. Furthermore, the intensity of magnon-polaron SSE is increased as Bi amount x increases, which is attributed to the enhanced MEC.[152]

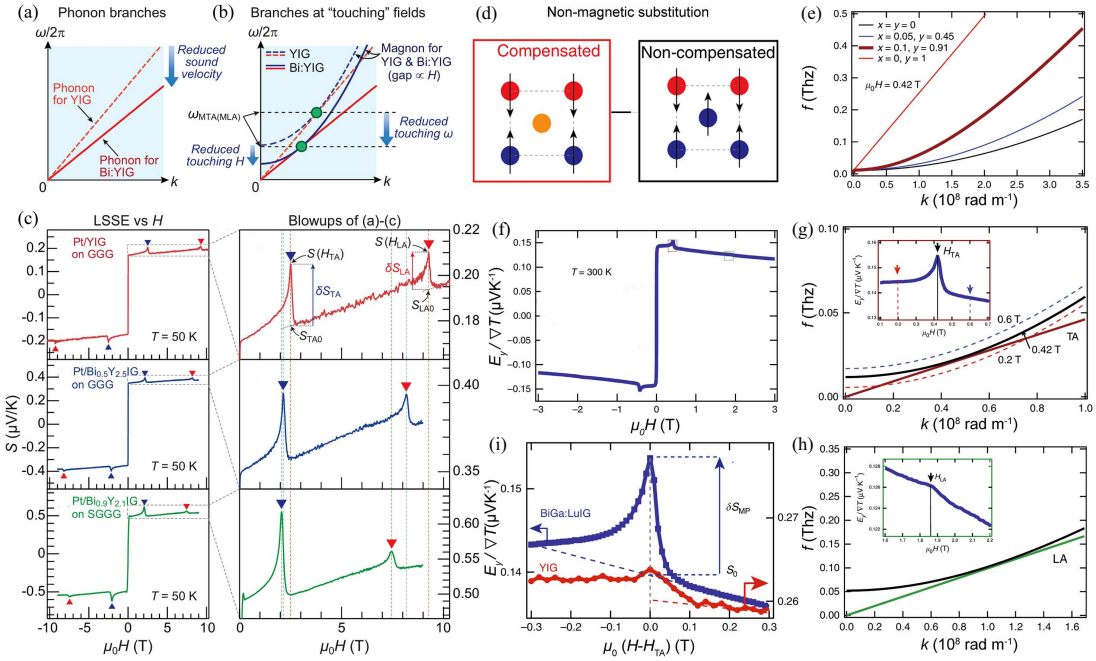


Fig. 8. (a) The phonon dispersion relations for YIG and Bi:YIG. (b) The magnon and phonon dispersion relations for YIG and Bi:YIG at the touching fields. (c) $\boldsymbol{H}$ dependence of the LSSE coefficient S for $Bi_xY_{3-x}IG$/Pt samples, for $x = 0$, 0.5, and 0.9 at $T = 50$ K. The magnified views around the anomaly fields are displayed at the right plane. The blue and red triangles represent magnon-polaron peaks at $\boldsymbol{H}_{\rm TA}$ and $\boldsymbol{H}_{\rm LA}$, respectively. Reprinted with permission from Ref. [72]. Copyright 2022 by American Physical Society. (d) Schematic of the non-magnetic substitution. (e) The magnon dispersions for different magnetic compensation effects. (f) $\boldsymbol{H}$ dependence of the SSE thermopower measured at 300 K in $(Lu_2Bi)Fe_4GaO_{12}$. The magnon and phonon dispersions at the red and green boxes correspond to (g) and (h), respectively. (i) Comparison of the peaks of the MPs at $\boldsymbol{H}_{\rm TA}$ for YIG and $(Lu_2Bi)Fe_4GaO_{12}$ at 300 K. Reprinted with permission from Ref. [38]. Copyright 2022 by Springer Nature.

Besides the tuning of the phonon spectrum, modifying the magnon spectrum via magnetic compensation offers an alternative pathway for tuning MPs. By non-magnetic ions Bi and Ga co-doping in LuIG (lutetium iron garnet), the Bi occupies the c-sites originally occupied by non-magnetic Lu, while Ga occupies the Fe-sites, resulting in the reinforced magnetic compensation of the system (Fig. 8(d)). Ga preferentially occupies the d-sites of Fe rather than the a-sites, and $Lu_2Bi[Ga_xFe_{2-x}](Ga_yFe_{3-y})O_{12}$ is formed, where x (y) denotes concentrations of the nonmagnetic ions Ga in a- (d-) sites. As magnetic compensation is introduced into the system, a transition from an uncompensated state ($x = y = 0$, analo-

gous to a ferromagnet) to a fully compensated state ($x = 0$, $y = 1$, equivalent to an antiferromagnet) can be realized (Fig. 8(e)). Correspondingly, the magnon dispersion curve will gradually transform from a ferromagnetic-like parabolic k-dependence (black curve) into an antiferromagnetic-like linear dependence, as shown in Fig. 8(e).[38] Under ideal conditions, in the antiferromagnetic state in which the group velocity of magnon dispersion matches sound velocity, magnon–phonon coupling effects can be maximized even further owing to the potential for more significant overlap between magnon and phonon dispersions. Theoretical model calculated magnon dispersions under different degrees of magnetic compensation, and $x = 0.1$, $y = 0.9$ are conformed, which is also consistent with the BLS experiments.[54] The magnon-polaron anomalies are observed at 0.42 T ($\boldsymbol{H}_{\rm TA}$) and 1.86 T ($\boldsymbol{H}_{\rm LA}$) in $(Lu_2Bi)Fe_4GaO_{12}$ at 300 K (Figs. 8(f)–8(h)). The small magnitudes of $\boldsymbol{H}_{\rm TA}$ and $\boldsymbol{H}_{\rm LA}$ are attributed to an increased magnetic compensation that makes the magnon dispersion steeper compared with the YIG and Bi:YIG case,[35,36,50,72] which leads to the touching condition between the magnon and phonon dispersions at lower $\boldsymbol{H}$. Meanwhile, a stronger magnetic compensation effect makes the magnon dispersion steeper, which significantly reduces the overlap between their magnon–phonon dispersions at the touching points (Figs. 8(g) and 8(h)). However, interestingly, the intensity of magnon-polaron peak at $\boldsymbol{H}_{\rm TA}$ is $\sim 700\%$ greater than that observed in YIG (Fig. 8(i)). This is attributed to the reduction of magnon lifetime of $(Lu_2Bi)Fe_4GaO_{12}$ compared to YIG and a larger ratio between the magnetic and acoustic quality of the crystal ($\eta \geq 1$) is obtained. Therefore, a greater enhancement of the lifetime of magnons by hybridization with the phonons at the touching points results in a greater SSE enhancement.[38]

3.2. Magnon polarons in compensated ReIGs

Rare-earth iron garnets (ReIGs, $Re_3Fe_5O_{12}$), with the prototype YIG as the most prominent member, represent an unparalleled material class for investigating strong magnon–phonon coupling and the ensuing formation of MPs. The M–T curve of YIG (Fig. 9(a)) obeys the Bloch law and the absence of compensation temperature ($T_{\rm comp}$). Therefore, the S–T of YIG (Fig. 9(b)) does not undergo a sign change. The lowest frequency mode of YIG is almost always modeled as a single ferromagnetic-like magnon dispersion.[153–155] At low temperatures, only the positive polarized mode is occupied, but at high temperature, the negative polarized mode plays a significant role. The suppression of S at high temperature (Fig. 9(c) @300 K) is due to thermally pumped magnons with opposite polarization to the positive polarized mode. As shown in Fig. 9(d), $Gd_3Fe_5O_{12}$ (GdIG) possesses two chiral magnons (α and β in Fig. 9(e)), which can be selectively excited by controlling temperature owing to temperature-sensitive moment and interaction relevant to the Gd sublattice.[21,68,71,100,145,146,156,157] The antiparallel aligned $\boldsymbol{M}_{\rm Gd}$ and $\boldsymbol{M}_{\rm Fe}$ exhibit different temperature-dependent characteristics, leading to the emergence of a $T_{\rm comp}$ in GdIG[146] (upper panel in Fig. 9(g)). When $T > T_{\rm comp}$, the $\boldsymbol{M}_{\rm Gd}$ becomes negligible, making the SSE response of GdIG similar to that of YIG, namely being dominated by the lowest Fe-dominated β-magnon branch[146] (lower panel in Fig. 9(g)). When the temperature reduces across the $T_{\rm comp}$, all magnetic moments flip (Fig. 9(f)), leading to a sign change of the SSE signal,

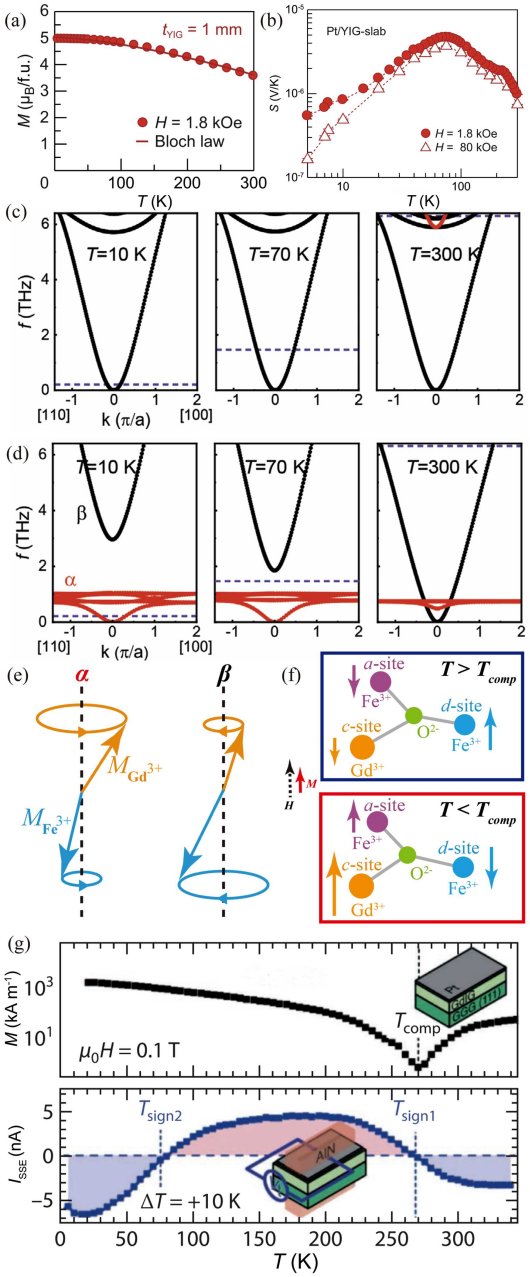


Fig. 9. (a) M–T and (b) S–T curves of YIG. Reprinted with permission from Ref. [158]. Copyright 2015 by American Physical Society. Calculated spin wave spectra of (c) YIG and (d) GdIG at various temperatures. Reprinted with permission from Ref. [100]. Copyright 2025 by Wiley-VCH GmbH. The α (red) and β (black) modes correspond to the (e) right- and left-handed magnons, respectively. (f) The three different magnetic sublattices of GdIG are shown for $T > T_{\rm comp}$ and $T < T_{\rm comp}$. (g) Temperature-dependent magnetization and SSE signal of GdIG. Reprinted with permission from Ref. [146]. Copyright 2016 by Springer Nature.

but the β-magnon branch still dominates SSE. When the temperature decreases further (Fig. 9(d) @10 K), there is a second sign change once the contribution from the Gd-dominated α-magnon branch overcomes that from the β-magnon branch[146] (lower panel in Fig. 9(g)).

The theoretical and experimental works on the magnon-polaron SSE of GdIG have been reported successively.[68,71] Shen reported theoretically that the longitudinal spin Seebeck coefficient (SSC) ζ_{xx} as a function of the $\boldsymbol{H}$ at different temperatures exhibits two types of magnon-polaron anomalies (Fig. 10(a)): (i) from 80 K to 120 K region, the magnon-polaron signal exhibits a single peak and its intensity dramatically increases; (ii) single-peak splits into double-peak as the temperature increases further and becomes more pronounced at 150 K.[68] The $\boldsymbol{H}$-driven dispersion relations reveal that the α-mode magnon is tangent to the TA phonon only once at 3.26 T for 120 K, while for 150 K, it is twice at 2.1 T and 2.5 T (Fig. 10(b)).[68] Differing from the double peaks related to MPs of the TA and LA phonon in YIG case, the double-peak structure originates from the α-magnon branch, which is tangent solely to the TA phonon dispersion.[35,68] From a holistic perspective, this is attributed to the distortion of the α-mode magnon dispersion driven by thermal magnon excitation. As a result, the group velocity v_{m} (the derivative of the dispersion curve) of the α-magnon dispersion is depicted as an inverted U-shaped parabola in k (Fig. 10(c)). At "touching" point, the magnon and phonon dispersions must share the same group velocity ($v_{\mathrm{m}} = v_{\mathrm{t}}$). Below $\sim$ 60 K, v_{m} is much smaller than the v_{t} at any k, meaning that there is no tangential relationship under any $\boldsymbol{H}$ and the absence of the magnon-polaron anomaly discussed above. As temperature increases, the v_{m}–k curve is lifted and gradually approaches v_{t}, resulting in that a single-peak anomaly appears and the magnon–phonon coupling strength increases from weak to strong. The single-peak intensity reaches its maximum at $\sim$ 108 K, where the tangential situation occurs ($v_{\mathrm{m}} = v_{\mathrm{t}}$). With increasing temperature further, the group velocities of the magnon and TA phonon have two crossing points (A and B) at k_{A} and k_{B}, meaning that α-magnon branch becomes tangential to the TA-phonon dispersion twice at $\boldsymbol{H}_{\mathrm{A}}$ and $\boldsymbol{H}_{\mathrm{B}}$ (Fig. 10(d)), finally giving double-peak structure. The distance between A and B gets larger with increasing temperature because of the upward shift of the v_{m}–k curve, which suggests that the double-peak splitting becomes increasingly pronounced. The single-peak to double-peak features at different temperatures of magnon-polaron anomaly in GdIG are also further confirmed by the SSE experiment[71] (Fig. 10(e)).

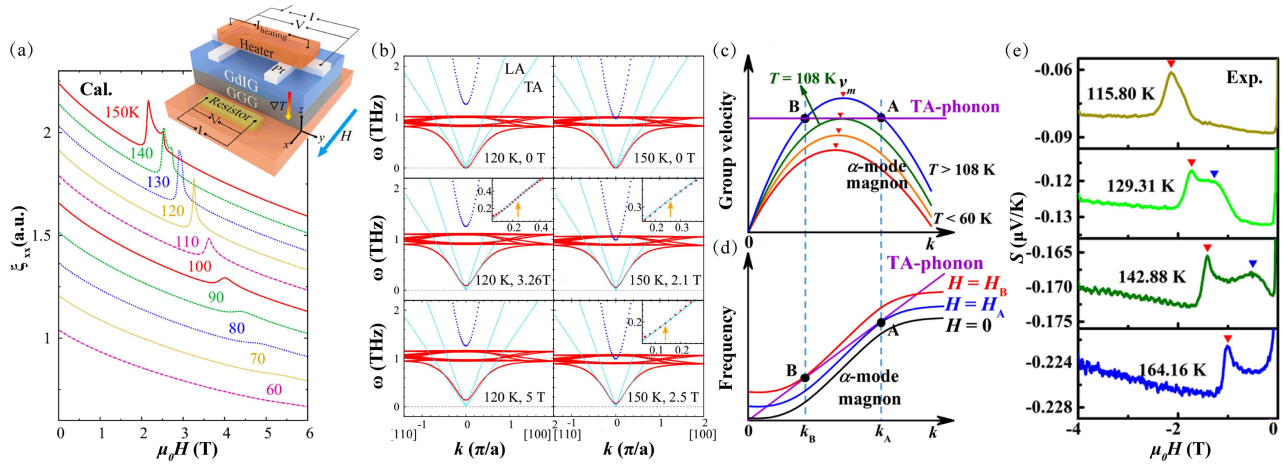


Fig. 10. (a) The SSC as a function of $\boldsymbol{H}$ at various temperatures. (b) Spin wave spectra at 120 K and 150 K with typical $\boldsymbol{H}$. The LA and TA phonons with sound speeds $C_{\mathrm{L}} = 6.50$ km/s and $C_{\mathrm{T}} = 3.39$ km/s,[159] respectively. Reprinted with permission from Ref. [68]. Copyright 2019 by American Physical Society. (c) The schematic diagram of the group velocities of the α-mode magnon and TA phonon as a function of k at different temperatures of GdIG film. (d) The schematic diagram of dispersion relations of the α-mode magnon and TA phonon for $T >\sim 108$ K at 0, $\boldsymbol{H}_{\mathrm{A}}$, and $\boldsymbol{H}_{\mathrm{B}}$, respectively. (e) The SSC as a function of $\boldsymbol{H}$ of the GdIG/Pt sample measured at different temperatures. Reprinted with permission from Ref. [71]. Copyright 2021 by American Physical Society.

In addition to ReIGs mentioned above with the collinear magnetic structure between the $\boldsymbol{M}_{\mathrm{Re}}$ and $\boldsymbol{M}_{\mathrm{Fe}}$, a charming feature of ReIGs with Re-ions exhibiting strong crystal-field effects (like Tb-, Dy-, Ho-, Er-, Tm- and Yb-ions) is the observation of low-temperature non-collinear magnetic structures featuring "umbrella-like" arrangements of the $\boldsymbol{M}_{\mathrm{Re}}$.[160–168] $Tb_3Fe_5O_{12}$ (TbIG), as one of the most typical representatives of this series, has a relatively strong anisotropy and a large magnetostriction constant due to the nonzero orbital angular momentum of Tb ions,[169] which implies a potentially large MP-induced SSE anomaly.

For the LSSE measurement of the TbIG/Pt sample with $\boldsymbol{H}$ sweeping along the [100] axis (Fig. 11(a)) reported by Li *et al.*,[73] the $\boldsymbol{H}$ dependence of the SSC strongly relies on the temperature (Fig. 11(b)). At 207 K and 157 K, the SSC presents a common step-shaped sign change at the very small coercive field and saturates to nearly a constant in the high $\boldsymbol{H}$ range. Very interestingly, for 97.37 K, the SSC shows an additional sign change around $\pm$2 T, further followed by an unexpected hysteresis-like anomaly at $\sim \pm$6 T, where the SSC

is surprisingly magnified even by one order of magnitude with respect to the weak-field value. Such behaviors in TbIG/Pt are markedly distinct from minor MP-SSE anomalies mentioned above.[35–38,50,67,68,72] Lahoubi reported hysteretic minor loops in the bulk TbIG only sweeping $\boldsymbol{H}$ along the [100] crystal axis (Fig. 11(c)) in comparable $\boldsymbol{H}$ range of hysteresis-like SSC anomaly in Fig. 11(b), which is related to the transition of double-umbrella magnetic structure (DUMS) under $\boldsymbol{H}$.[161,165] The theoretical model by taking into account an effective on-site anisotropy of Tb atoms reproduces the hysteresis loop (Fig. 11(d)), the evolution of DUMS (Fig. 11(e)), and corresponding magnon spectra (Fig. 11(f)) with $\boldsymbol{H}$. At $\boldsymbol{H}_1$ (zero field), DUMS exhibits two conical structures with different cone angles, and each possesses three-fold rotational symmetry of $\boldsymbol{M}_{\rm Tb}$ around the [111] axis while the net $\boldsymbol{M}_{\rm Fe}$ along $[\bar{1}\bar{1}\bar{1}]$. The zero-field magnon spectrum is similar to that in GdIG,[68] except for a larger magnon gap of the lowest Tb-dominated α branch due to the strong anisotropy of the Tb atoms and anti-crossing features between the Fe-dominated β branch and those flat dispersion-less branches dominated by the Tb sublattices.[73] The high-$\boldsymbol{H}$ hysteresis loop results from the transition of the c_1' sublattice of $\boldsymbol{M}_{\rm Tb}$ when its effective anisotropic magnetic field is overcome by $\boldsymbol{H}_2$ and $\boldsymbol{H}_3$ (Fig. 11(e)). The magnon gap is reduced and finally vanishes at $\boldsymbol{H}_2$, where the SSE contribution from the α branch is enhanced significantly according to Bose–Einstein statistics and dominates over the contribution from the β branch with opposite polarization, explaining the low-field (~ 2 T) sign change at 97.37 K. More interestingly, the dispersion of the α branch at $\boldsymbol{H}_2$ becomes nearly parallel to the LA phonon dispersion in a quite wide momentum space in the low-frequency range (Fig. 11(f)), which suggests that the formation of a large number of MP states could also benefit the large enhancement of the SSE signal. At $\boldsymbol{H}_3$, the α branch experiences a drastic uplift, leading to a remarkable reduction in its contribution to SSE and hence a sharp jump anomaly. Moreover, the hysteresis behavior completely vanishes in the same TbIG/Pt sample when the $\boldsymbol{H}$ is applied along the [110] or [111] axis (Fig. 11(g)), which is consistent with M–H in Fig. 11(c).

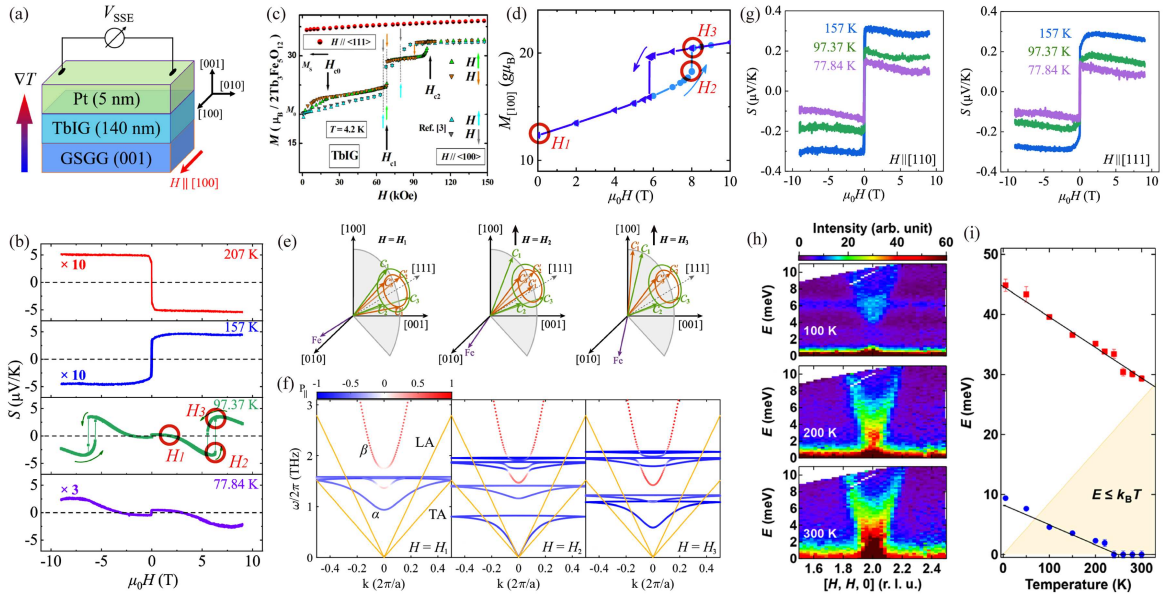


Fig. 11. (a) The schematic for LSSE measurements in the TbIG/Pt sample with $\boldsymbol{H}$ sweeping along the [100] axis. (b) SSC as a function of $\boldsymbol{H}$ at typical temperatures. Reprinted with permission from Ref. [73]. Copyright 2024 by American Physical Society. (c) $\boldsymbol{M}$–$\boldsymbol{H}$ curves of bulk TbIG at 4.2 K. Reprinted with permission from Ref. [165]. Copyright 2012 by Institute of Physics Publishing. (d) The simulated total magnetization $\boldsymbol{M}_{[100]}$ as a function of the sweeping $\boldsymbol{H}$ in the [100] direction. (e) Schematic diagram of the DUMS at $\boldsymbol{H}_1$, $\boldsymbol{H}_2$ and $\boldsymbol{H}_3$. The c_1, c_2 and c_3 (c_1', c_2' and c_3') represent $\boldsymbol{M}_{\rm Tb}$ located umbrella with larger (smaller) cone angle. c_1 and c_1' are located in the $(0\bar{1}1)$ plane. (f) The magnon spectra of bulk TbIG in the low-frequency regime (< 3.1 THz) at $\boldsymbol{H}_1$, $\boldsymbol{H}_2$ and $\boldsymbol{H}_3$. The LA and TA phonons with sound speeds $C_{\rm L} = 6.08$ km/s and $C_{\rm T} = 3.3$ km/s,[170] respectively. (g) The SSC as a function of the $\boldsymbol{H}$ along [110] and [111] directions, respectively. Reprinted with permission from Ref. [73]. Copyright 2024 by American Physical Society. (h) Measured spectra for low-energy magnon mode taken at 100 K, 200 K, and 300 K. (i) Temperature dependence of the estimated gap energies for high-energy (red square) and low-energy magnon modes (blue circle). The shaded area marks $E \le k_{\rm B}T$. Reprinted with permission from Ref. [171]. Copyright 2024 by American Institute of Physics Publishing.

Kawamoto *et al.* adopted INS to measure temperature dependence of the magnon modes for bulk TbIG sample.[171] Compared to the degenerate energy band at 200 K and 300 K, the low-energy dispersion relations with finite energy gaps are observed at 100 K due to the strong anisotropy of the Tb atoms (Fig. 11(h)),[171] which is consistent with calculations (Fig. 11(i)).[73] Compared to GdIG, the large gap of the α branch in TbIG suppresses the thermal excitation of this magnon branch and hence restrains its contribution to the SSE, which may be the reason for the absence of the second sign change in the temperature dependence of the SSE signal below $T_{\rm comp}$ (Fig. 12(a)).[75] The estimated gap energies for the high-energy (β, red square) and low-energy magnon modes (α, blue circle) exhibit an obvious decrease with increasing temperature, and the low-energy magnon mode almost disappears above 200 K.[171] Furthermore, the $\boldsymbol{M}_{\rm Tb}$ starts to obtain

noncollinearity and form DUMS below 160 K, whereas the umbrella angle becomes almost zero, and a collinear magnetic structure is formed above 160 K. These results indicate that the anisotropy of the Tb atoms is significantly dominant (diminished) at low (high) temperatures. Li *et al*. reported that, within a narrow range slightly below $T_{\rm comp}$, SSE anomalies with dip shape were observed near zero field, as indicated by green arrows in Fig. 12(b). Theoretical calculations almost reproduce the MP-anomaly feature observed in the experiment (Fig. 12(c)). The evolution of dispersion relations with $\boldsymbol{H}$ revealed that the dispersion of α branch magnon only has a single intersecting point with LA phonon in the relatively low-frequency range at $H = H_2$ in Fig. 12(d), leading to abundant magnon-polarons states contributing to the single peak MP-anomaly of the SSE signal.[75] It is valuable to point out that although the dispersions look very similar to GdIG,[68] the suitable group velocity induces the parallel relation between the α branch and LA phonon rather than the TA phonon.[75]

The $\boldsymbol{M}_{\rm Tb}$ and $\boldsymbol{M}_{\rm Fe}$ flip when crossing $T_{\rm comp}$.[172–174] Within a narrow temperature range slightly above the $T_{\rm comp}$, the $\boldsymbol{M}_{\rm Tb}$ and $\boldsymbol{M}_{\rm Fe}$ are nearly equal, and spin-flop (SF) transition will occur when $\boldsymbol{H}$ obtains a critical value. The evolution process of $\boldsymbol{M}_{\rm Tb}$ and $\boldsymbol{M}_{\rm Fe}$ with $\boldsymbol{H}$ and $\boldsymbol{T}$ was interpreted by SSE.[75] The calculated negative value of the projection of the net $\boldsymbol{M}_{\rm Fe}$ in the $\boldsymbol{H}$ direction possesses very similar curve shapes to the SSC–$\boldsymbol{H}$ curves in measurement (Fig. 12(e)), suggesting that the reorientation of the equilibrium net $\boldsymbol{M}_{\rm Fe}$ is the key to the observed SSC feature. From the phase diagram (Fig. 12(f)), the complete evolutionary process of the $\boldsymbol{M}_{\rm Tb}$ and $\boldsymbol{M}_{\rm Fe}$ sublattices can be intuitively observed, in which $\boldsymbol{M}_{\rm Fe}$ and $\boldsymbol{M}_{\rm Tb}$ form a noncollinear canting magnetic structure. This work reveals that $\boldsymbol{H}$ can highly tune the flipping process of the different sublattices in TbIG near $T_{\rm comp}$, allowing for continuous tunability of SSC in the TbIG/Pt heterostructure.[75] More importantly, this tunable effect can be achieved near zero magnetic field, which holds promise for the development of ReIG-based low-power magnon spintronic devices. Moreover, the anomalous behaviors of the SSE within a relatively complete range below 300 K in TbIG reported by Li *et al*. demonstrated that SSE is a promising probe for interpreting magnon transport with complex spin structures.[73,75]

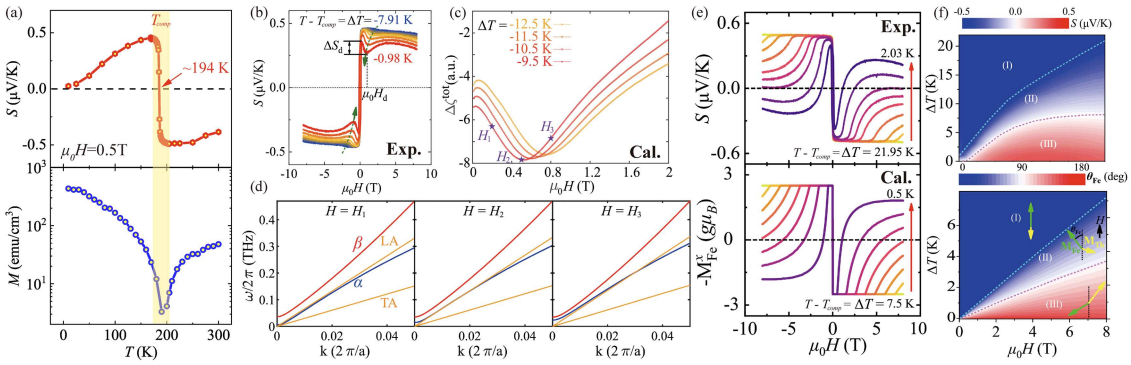


Fig. 12. (a) SSC–T and $\boldsymbol{M}$–T curves. (b) SSC as a function of the $\boldsymbol{H}$ immediately below the $T_{\rm comp}$. (c) The calculated SSC enhancement due to MPs as a function of the $\boldsymbol{H}$ below the $T_{\rm comp}$. (d) Magnon spectra of bulk TbIG in the low-frequency regime (< 0.5 THz) for $\Delta T = -9.5$ K and three typical $\boldsymbol{H}_1$, $\boldsymbol{H}_2$, and $\boldsymbol{H}_3$ denoted in (c). The LA and TA phonons with sound speeds $C_{\rm L} = 7.2$ km/s and $C_{\rm T} = 3.3$ km/s,[170] respectively. (e) Experimental results of SSC and the calculated negative value of the projection of the net $\boldsymbol{M}_{\rm Fe}$ in the $\boldsymbol{H}$ direction as functions of $\boldsymbol{H}$ at typical temperatures above the $T_{\rm comp}$. (f) The $\boldsymbol{H}$–ΔT phase diagrams of SSC and $\theta_{\rm Fe}$ (the angle between $\boldsymbol{M}_{\rm Fe}$ and $\boldsymbol{H}$) for more refined temperatures mapping at the positive field region, corresponding to (e). The orientations of magnetization vectors $\boldsymbol{M}_{\rm Fe}$ and $\boldsymbol{M}_{\rm Tb}$ in different phases are shown schematically by green and yellow arrows in (f), respectively. Reprinted with permission from Ref. [75]. Copyright 2025 by Springer Nature.

3.3. Magnon polarons in antiferromagnetic insulators

Unlike their ferromagnetic counterparts, antiferromagnetic (AFM) magnons are characterized by a two-sublattice structure with opposing magnetic moments, resulting in a compensated net magnetization. This fundamental characteristic confers several distinct advantages. First, AFM magnons typically operate in the terahertz (THz) frequency regime,[81,82,85,175,176] orders of magnitude higher than the GHz frequencies of ferromagnetic magnons, which is critical for high-speed information processing.[177–179] Secondly, the stray-field-free nature of AFMs enables ultra-dense device integration with minimal cross-talk.[177] Furthermore, AFM magnons exhibit remarkable dynamic phenomena, such as a strong coupling to the Néel vector, which allows for efficient manipulation via electrical currents through spin–orbit torques.[16,18–20,84] AFM magnons have emerged as promising candidates for next-generation spintronic and magnonic applications because of their unique properties.[19,83,180–185] However, magnon transport in AFMs remains largely unexplored due to the presence of two spin sublattices and multiple easy axes, which induce more complex magnon modes than those in FMs.

Cr_2O_3 is one of the typical uniaxial AFM insulators, featuring a relatively simple spin structure with its easy axis aligned along the c-axis of the hexagonal lattice[82,177,187,188] (Fig. 13(a)). The accessible AFM resonance frequency (about 0.165 THz at 0 K) and SF field ($\boldsymbol{H}_{\rm SF} = 6.0$ T at 0 K) of Cr_2O_3 offer it opportunities to explore the properties of its magnon transport,[69,82,129,144,189,190] including magnon gen-

eration, transport, and detection. Recent key advances reported by Li *et al.* have confirmed this, showing that magnon transport in Cr_2O_3 has been explored via the SSE and spin pumping,[69,82] alongside the observation of its MPs[69] (Fig. 13(b)).

Figure 13(c) shows the evolution of magnon energy E with $\boldsymbol{H}$ for different magnon modes at $k = 0$.[69] Unlike only α-mode magnon in FMs, there are two distinct eigenmodes (the m-1 and m-2 modes correspond to the α and β modes, respectively.) of AFM magnon branches carrying equal but opposite angular momenta below the H_{SF}, as depicted in Fig. 13(d), and they are degenerate at $\boldsymbol{H} = 0$. At this point, the AFM magnon dispersion exhibits approximately a straight line in E–k space and lies well above those of acoustic phonons (Fig. 13(e)). The degeneracy between α and β modes is lifted by applied $\boldsymbol{H}$ along the c axis of Cr_2O_3. The dispersion of α mode moves up, thereby cannot reach the tangential condition with acoustic phonons, while dispersion for β mode continuously shifts down with increasing $\boldsymbol{H}$ and intersects those of LA and TA phonons before SF transition (Fig. 13(e)). When $\boldsymbol{H}$ reaches the H_{SF}, spins in both sublattices rotate abruptly to be nearly perpendicular to $\boldsymbol{H}$ with a small inclination. Both α and β modes are replaced by two new m-3 and m-4 modes, where m-3 mode has the RH chirality, but the m-4 mode does not carry angular momentum (Fig. 13(d)). Among these complex magnon modes, only β mode has a chance to be successively tangent to the LA and TA phonon branches at $\mu_0 H_{LA}$ and $\mu_0 H_{TA}$ when $\boldsymbol{H}$ gradually increases. The results of SSE measurements for both Cr_2O_3/Ta and Cr_2O_3/Pt heterostructures exhibit opposite $\boldsymbol{H}$ dependence due to the opposite spin Hall angle (Fig. 13(g)), and the SSE anomalies appear due to the MPs after properly subtracting the smooth background (Fig. 13(h)). The SSE anomalies exhibit as peaks for both LA and TA MPs, indicating that AFM magnons suffer stronger scattering than phonons do ($\eta > 1$), leading to an enhancement in SSE magnitude. Furthermore, note that the SSE experiences an abrupt jump and sign reversal at $\boldsymbol{H}_{SF}$, which is correlated with the magnon mode switching from β mode to m-3 mode and accompanied by spin polarization switching. Above H_{SF}, the magnon dispersion of the m-3 mode no longer intersects with acoustic phonon dispersions, while the magnon dispersion of m-4 mode is independent of the $\boldsymbol{H}$ and intersects with acoustic phonon dispersions only at $k = 0$, which does not form MPs (Fig. 13(f)).

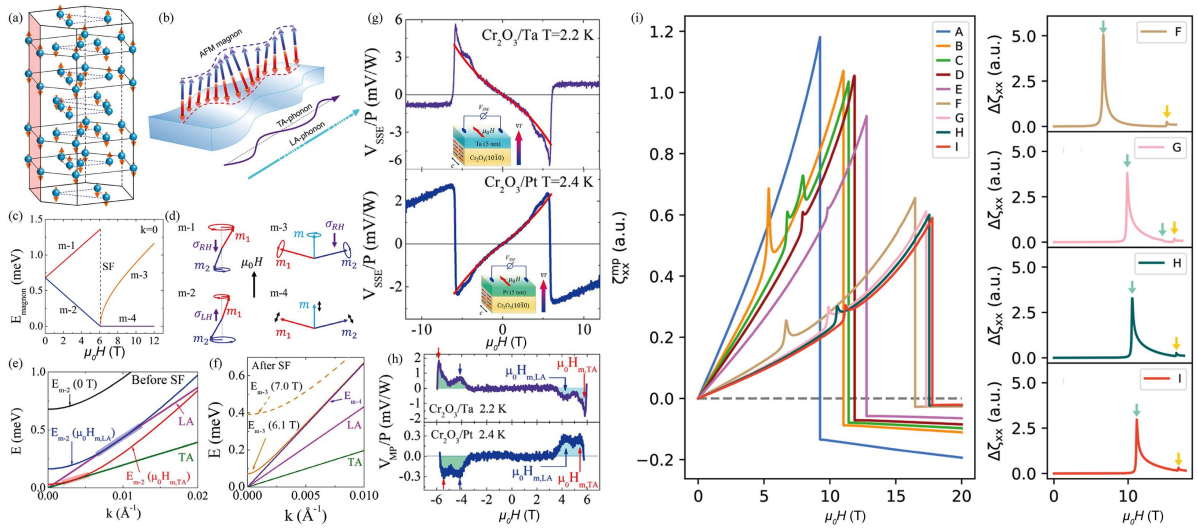


Fig. 13. (a) Crystal structure of Cr_2O_3. (b) Schematic diagram of MPs in real-space for uniaxial antiferromagnet. (c) Magnon modes of Cr_2O_3, corresponding to (d), in E (magnon energy)–H space for $k = 0$. The magnon and acoustic phonon dispersions of Cr_2O_3 before (e) and after (f) SF. (g) SSE signals V_{SSE}/P in Cr_2O_3/Ta (at 2.2 K) and Cr_2O_3/Pt (at 2.4 K), and (h) magnon-polaron signals V_{MP}/P after subtracting the background from the original SSE signals in (g). Reprinted with permission from Ref. [69]. Copyright 2020 by American Physical Society. (i) Calculated magnon-polaron signals as a function of the $\boldsymbol{H}$ along the easy axis of uniaxial AFMs for different conditions of the anisotropy field and exchange interaction field. Reprinted with permission from Ref. [186]. Copyright 2022 by American Institute of Physics Publishing.

Recent theoretical work reported by Liu *et al.* systematically analyzed the evolution of the magnon spectrum and the MP-induced anomaly in the SSE in the uniaxial easy-axis AFM insulator with a body-centered cubic structure with varying $\boldsymbol{H}$, strength of exchange interaction, and magnetic anisotropy.[186] The sudden sign reversal of SSC–$\boldsymbol{H}$ curves happened at the SF transition. The MP anomaly was indeed absent above H_{SF}, whereas it was only observed in the relatively weak $\boldsymbol{H}$ regime before the SF transition (Fig. 13(i)). All these features are highly similar to those observed in SSE measurement above in Cr_2O_3.[69] The interesting aspect is that, for different values of the anisotropy field and exchange interaction field, the MP anomaly exhibits one, two, and even three peaks (A to I curves in Fig. 13(i)). For scenario B, one MP peak shows up due to the interaction between the β magnon and TA phonon, and it splits into two peaks at scenario C, which is quite similar to that in GdIG as to temperature-driven group velocities of magnons, as shown in Figs. 10(c) and 10(d).[68,71] Even though two MP peaks appear for all scenarios of F, H, and I, the yellow (light blue) arrows refer to the

anomalies caused by the interaction between β magnon and TA (LA) phonon. The LA-phonon-associated peak at F splits into two peaks at G, meanwhile addition of TA-phonon-related peak, eventually leads to a triple-peaks feature.[186]

3.4. Topological magnon polarons in multiferroic materials

Multiferroic materials are characterized by strong interactions between magnetic order and lattice degrees of freedom, making them an ideal platform to investigate the coupling between magnons and phonons. In this context, $Fe_2Mo_3O_8$ (FMO) has emerged as a material of significant interest. FMO crystallizes in a polar hexagonal structure (space group $P6_3mc$), featuring alternating layers of Fe^{2+} and Mo^{4+} ions[52,191,192] (Fig. 14(a)). This non-centrosymmetric crystal structure is intrinsically linked to its functional properties, hosting the necessary conditions for strong magneto–elastic coupling. Magnetism arises primarily from the Fe^{2+} ions with honeycomb-like sublattices, which sit on two distinct sites with different magnetic moments in corner-shared tetrahedra and octahedra. Since both space inversion and time-reversal symmetries are broken, FMO orders in a collinear AFM with below the Néel temperature ($T_N \sim 60$ K), with a strong uniaxial (Ising-like) anisotropy forcing the Fe^{2+} spins to align along the c-axis. The absence of an inversion center between nearest-neighbor Fe sites allows for a non-zero in-plane Dzyaloshinskii–Moriya (DM) interaction (Fig. 14(a)). A key feature is the magnetoelectric coupling: the application of $\boldsymbol{H}$ along the c-axis can reverse the electric polarization, a phenomenon driven by the exchange striction mechanism within the non-centrosymmetric lattice. A colossal linear magnetoelectric effect is reported in polar magnet FMO.[193] Significant phenomena such as magnetoelectric coupling and thermal Hall effect exist in FMO, indicating a strong coupling between the spin and orbital degrees of freedom in the material, which provides favorable conditions for the formation of MPs (Fig. 14(b)).

Bao *et al.* directly probed high-resolution neutron spectroscopy and fully mapped out the magnon and phonon bands in large-sized FMO single crystals in momentum-energy space via INS experiments,[52] as shown in Fig. 14(c). The excitation spectra comprise various modes that can be categorized into three types. First, two magnon excitations are observed at high energies around 11 meV and 14 meV. These exhibit strong scattering intensity and weak dispersion, and are twofold degenerate, which agrees well with calculations from linear spin wave theory. Second, phonon excitations emerge at low energies, showing weak scattering intensity and strong dispersion — characteristics that contrast sharply with those of magnon excitations. Third, MPs occur as a result of the convergence and hybridization between high-energy magnon and phonon dispersions (Fig. 14(d)). The energy bands of the MPs can be clearly distinguished. Key features of these hybrid bands include the energy gap at the intersection of the originally uncoupled magnon and phonon dispersions, the mixing and conversion between magnon and phonon components, and band inversion. Without magnon–phonon coupling, the calculated magnon and phonon dispersions capture the main characteristics of the INS spectra (Fig. 14(c)) yet fail to reproduce the anticrossings (upper panel in Fig. 14(f)). When the magnon–phonon coupling induced by the DM interaction is taken into account, magnons and phonons hybridize in the high-energy region to form MPs, as depicted in the lower panel in Fig. 14(f), and the experimentally observed results can be successfully reproduced. This work comprehensively reveals the band structure of topological MPs, identifies anomalous low-energy phonon modes, and verifies a new magnon–phonon coupling mechanism, thereby establishing a new avenue for realizing topological states (Fig. 14(e)).

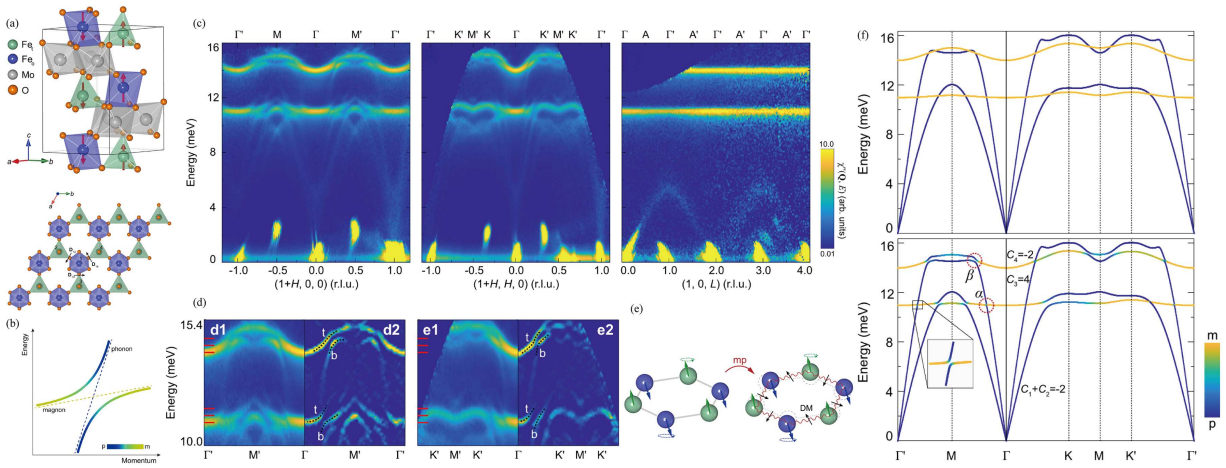


Fig. 14. (a) Crystal and magnetic structures of FMO in side view and top view. Red arrows indicate the magnetic moments on Fe atoms, and black arrows mark the in-plane DM vectors. (b) Schematic of the MPs at anticrossing of magnon and phonon bands. (c) and (d) Magnon-polaron excitation spectra measured by INS. (e) Schematic diagram for the DM-interaction-induced magnon–phonon coupling in FMO. (f) Calculations of the magnon-polaron bands for uncoupled magnons (orange) and phonons (blue) without the DM interaction, and topological MPs resulting from the DM-interaction-induced magnon–phonon coupling. Reprinted with permission from Ref. [52]. Copyright 2023 by Springer Nature.

3.5. Magnon polarons in 2D materials

The discovery and investigation of 2D magnetic materials have opened a new chapter in MPs.[61,194] They not only offer controllable dimensionality from the bulk down to the monolayer limit but also exhibit tunable magnon and phonon spectra under various external stimuli such as $\boldsymbol{H}$, temperature, and electric gating, providing a foundation for understanding and designing quantum devices based on spin–lattice hybridization.[195–197]

The strong coupling between magnons and phonons has been observed in vdWs AFM insulator transition metal phosphorus trichalcogenides (MPX_3, M = Fe, Mn, Ni, and X = S, Se), profiting from their entirely surface spins at the 2D limit and enhanced phonon amplitude along the out-of-plane direction.[198,199] Mai *et al.* observed the hybridization between E_g mode phonons and a two-magnon continuum in $MnPS_3$ via temperature-dependent Raman spectroscopy.[58] As shown in Fig. 15(a), upon cooling below T_N, the phonon frequencies exhibited substantial changes in intensity and frequency, while a new peak from the two-magnon continuum appeared and continued to increase in frequency. Asymmetric Fano line shape emerged, indicating strong coupling between the phonons and the magnon continuum and resulting in phonon frequency shifts and magnon lifetime reduction.[58] This work provides an identification of a magnon decoherence pathway via magnon–phonon hybridization in a 2D antiferromagnet.

The coupling of magnon and phonon can lead to the transfer of spin angular momentum. Liu *et al.* directly observed strong coupling between magnons and phonons in $FePS_3$ via magneto-Raman spectroscopy at $\boldsymbol{H}$ up to 30 T.[57] The peak at 121.5 cm^{-1} is identified as a Raman-active magnon that undergoes Zeeman splitting to $M_\uparrow$ and $M_\downarrow$ under an applied $\boldsymbol{H}$ (Fig. 15(b)). When this magnon is tuned into resonance with a nearby phonon mode, a typical anticrossing behavior is observed (Fig. 15(b)), signifying the formation of a hybrid MP. The energy dispersion is given by $\omega^{\pm} = \frac{-\omega_{M_\uparrow}+\Omega}{-2} \pm \frac{1}{2}\left[(\omega_{M_\uparrow} - \Omega) + 4|M_c|^2\right]^{1/2}$, where $\omega^{\pm}$ describe the energy dispersion of the two anticrossing bands. $\omega_{M_\uparrow}$ and Ω are the frequencies of magnons and phonons, respectively. The coupling strength M_c is 87.8 GHz, which is 2 orders larger than the ferromagnetic magnon.[200] Figure 15(c) shows the degree of circular polarization for transverse optical (TO) phonon (P_3) and magnons $M_\uparrow$ (and $M_\downarrow$) under different $\boldsymbol{H}$, the polarization behavior of $M_\uparrow$ and P_3 reverse, indicating the transfer of spin angular momentum from the magnon to the TO phonon via the strong coupling.

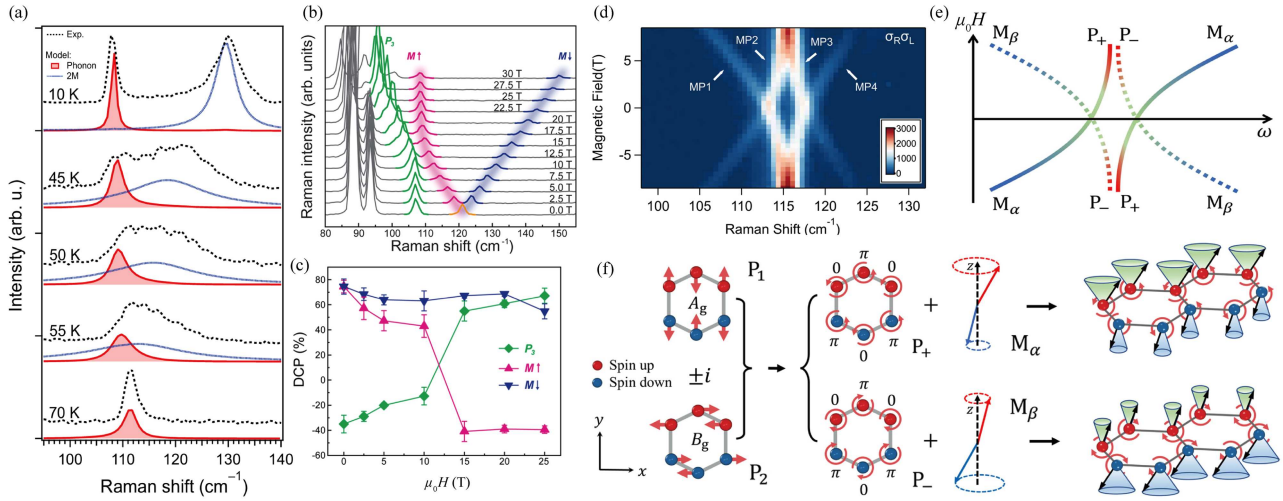


Fig. 15. The MPs in 2D AFMs. (a) Temperature-dependent Raman spectra of $MnPSe_3$, which can be well-fitted via the hybridization of two-magnon (2M, blue dash) and phonons (solid red filled). Reprinted with permission from Ref. [58]. Copyright 2021 by American Association for the Advancement of Science. (b) Raman spectra of $FePS_3$ under $\boldsymbol{H}$ from 0 to 30 T. Zeeman splitting of the M branch identifies it as a magnon mode. The two branches are denoted as $M\uparrow$ (red) and $M\downarrow$ (blue). (c) $\boldsymbol{H}$-dependent degree of circular polarization (DCP) of P_3 (green), $M\uparrow$ (red), and $M\downarrow$ (blue). Reprinted with permission from Ref. [57]. Copyright 2021 by American Physical Society. (d) Magneto-Raman spectra with RH circular excitation and LH detection ($\sigma_R\sigma_L$). (e) Schematic diagram of the MP branches under $\boldsymbol{H}$, where $P_\pm$ represent the chiral phonons and M_α and M_β represent two AFM magnon modes. (f) Schematic diagrams for the selective hybridization of chiral phonon $P_\pm$ with AFM magnons M_α and M_β. Reprinted with permission from Ref. [60]. Copyright 2023 by Springer Nature.

Furthermore, the chirality selectivity of magnon–phonon coupling is observed in $FePSe_3$.[60] In circular polarization-resolved magneto-Raman spectroscopy (Fig. 15(d)), the MPs in $FePSe_3$ split into 4 branches (MP1–MP4) as the $\boldsymbol{H}$ increases. MP1 and MP4 exhibit magnon-like characteristics and couple to chiral phonon-like branches MP2 and MP3, respectively. At zero field, the coupling strength reaches 60 GHz and survives down to the quadrilayer limit. Cui *et al.* established a coupling model to uncover the chirality-selective magnon–phonon hybridization.[60] As illustrated in Figs. 15(e) and 15(f), a pair of degenerate phonon modes, P_1 and P_2, coherently superpose in phase to form degenerate chiral phonons P_+ and P_-. The magnon–phonon coupling induces the degeneracy of P_+ and P_- lifted under $\boldsymbol{H}$. Specifically, P_+ (P_-) couples exclusively with the magnon mode M_α (M_β) that possesses the same angular momentum

direction. This selective coupling is dictated by the nonsymmorphic screw axis symmetry of $FePSe_3$, which restricts phonon coupling to magnons via specific magnetic anisotropy terms, thereby enabling hybridization conditioned on angular momentum matching. These results establish a platform for exploring entangled magnon–phonon–photon cavity systems, implying the potential of 2D antiferromagnet in angular momentum encoded quantum information and simulation.

4. Applications and devices

4.1. Surface acoustic wave devices for magnon–phonon coupling

Magneto–acoustic coupling describes the interaction between magnetic order and acoustic waves (mechanical vibrations) in materials. Central to this phenomenon is the magnetostriction effect, whereby an applied $\boldsymbol{H}$ alters the magnetization of material, inducing lattice strain that generates or modifies acoustic waves. Conversely, incoming acoustic waves produce stress that shifts magnetization via the inverse magnetostriction effect — enabling detection of magnetic changes. This coupling enables diverse applications across multiple fields. In sensing, it facilitates highly sensitive magneto-acoustic surface wave sensors for non-contact current monitoring and magnetic tag detection. In data storage, acoustic-wave-assisted recording schemes exploit localized sound to lower the switching energy barrier for higher-density storage. Electromagnetic devices such as acoustic delay lines and tunable filters utilize magnetic control over wave propagation, serving as key components in radar and communications. Moreover, in fundamental science, magneto–acoustic coupling provides a valuable means to probe magnetic properties and manipulate magnon dynamics. The surface acoustic waves (SAWs) serve as a particularly efficient and versatile platform for exploring and harnessing magneto–acoustic coupling.[28,201–205] The MHz–GHz frequency range of SAWs is inherently compatible with that of ferromagnetic resonance (FMR), providing a foundational basis for designing integrated magneto-acoustic devices. SAWs can be readily generated and detected using interdigital transducers (IDTs), making them ideal for integrated device applications. Their associated dynamic strain fields interact directly with magnetic moments via magnetostriction, enabling effective excitation and manipulation of spin waves.

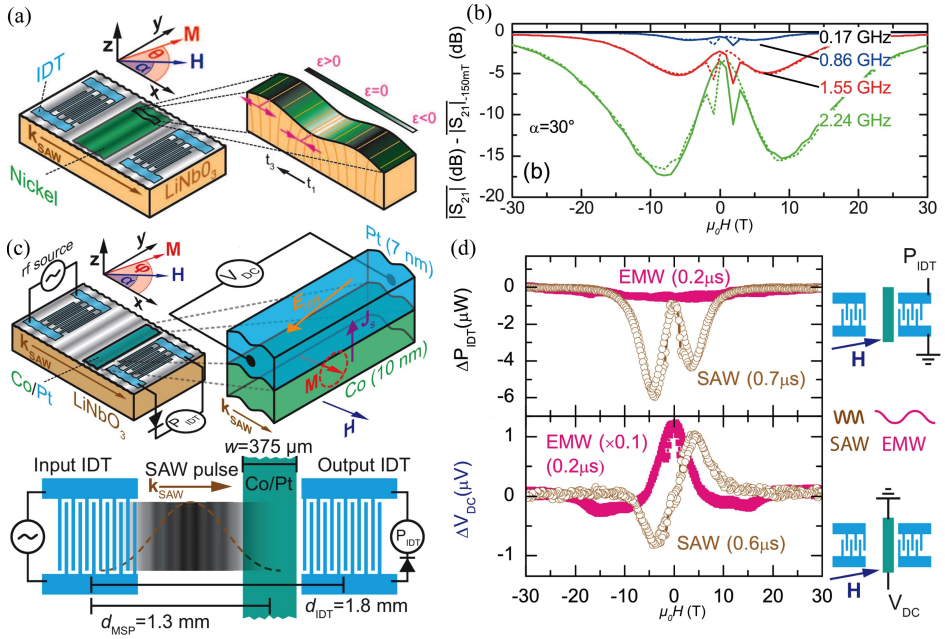


Fig. 16. (a) SAWs are excited and detected by FMR in Ni/$LiNbO_3$ hybrid device. (b) $\boldsymbol{H}$ dependence of SAW transmission at different frequencies. Reprinted with permission from Ref. [77]. Copyright 2011 by American Physical Society. (c) Spin pumping with SAWs in $LiNbO_3$/Co/Pt. (d) SAW power difference and ΔV_{DC} for the detection of the SAW and the EMW pulses at the bilayer at the output IDT as a function of $\boldsymbol{H}$. Reprinted with permission from Ref. [206]. Copyright 2012 by American Physical Society.

In 2011, Weiler *et al*. reported that SAWs are capable of exciting FMR through magnon–phonon interactions in a thin magnetic film deposited on a piezoelectric substrate.[77] Their work utilized GHz-frequency SAWs to achieve all-elastic excitation and detection of FMR in a ferromagnetic/ferroelectric (Ni/$LiNbO_3$) hybrid structure (Fig. 16(a)). Notably, the experiments were conducted without applying an external radiofrequency magnetic field to the ferromagnet, thereby confirming that the FMR excitation was acoustically driven via MEC between the SAW-induced strain field and the magnetic layer (Fig. 16(b)). Their subsequent work revealed the ability to generate spin currents at RT by exploiting resonant phonon–magnon coupling through phonon-driven spin pumping,[206] using 1.55-GHz, 300-ns SAW pulses to provide coherent elastic waves in a Co/Pt bilayer (Fig. 16(c)). The IDT simultaneously excites electromagnetic waves (EMWs), which can be distinguished from SAWs in the time domain. When $\boldsymbol{H}$ is tuned to the resonance condition (±4 mT), the transmitted

SAW power (ΔP_{IDT}) decreases significantly, indicating that the attenuated SAW power is absorbed by FMR (Fig. 16(d)). Under FMR conditions, the reversal of the magnetic field direction leads to a sign change in the ΔV_{DC} signal, which is a characteristic signature of the ISHE. This synergy not only facilitates the investigation of fundamental magnon–phonon interactions but also underpins the operation of modern magnetoacoustic devices, such as filters, resonators, and sensors.

4.2. Long-distance propagation of magnon polarons

Utilizing the coupling between SAWs and spin waves to enhance the decay length of magnon is an important research direction. Zhang *et al*. demonstrated ultra-long magnon decay lengths up to 1 mm at RT in BFO/$La_{0.67}Sr_{0.33}MnO_3$ (LSMO) heterostructures (Fig. 17(a)) — more than two orders of magnitude longer than that of bare metallic LSMO films.[78] This remarkable enhancement is attributed to the formation of MPs, hybrid excitations resulting from the MEC between magnons in the ferromagnetic LSMO layer and phonons in the multiferroic BFO layer (Fig. 17(b)). Using angle-resolved propagating spin-wave spectroscopy (AR-PSWS) and time-resolved Brillouin light scattering (TR-BLS), they identify two distinct spin-wave modes: a conventional Damon–Eshbach mode (Mode Y) with a decay length of ~ 5 μm and a group velocity of ~ 0.8 km/s, and a hybrid magnon–phonon mode (Mode X) exhibiting a high group velocity of $\sim$2.5 km/s and a millimeter-scale decay length (Figs. 17(c) and 17(d)). Theoretical simulations incorporating effective MEC quantitatively reproduce the observed anticrossing behavior and long-range propagation (Figs. 17(e) and 17(f)). This work offers a viable pathway to overcome the intrinsic damping limitations in metallic magnonic systems and opens new opportunities for designing low-loss, high-speed hybrid magnonic devices. In 2023, Wang *et al*. demonstrated the coherent propagation of MPs, hybrid excitations resulting from the coupling between spin waves and Rayleigh/Love SAWs (Fig. 17(g)), in a ferroelectric $BaTiO_3$ (BTO) and ferromagnetic LSMO heterostructure.[79] Using IDTs, both Rayleigh (longitudinal acoustic, LA) and Love (transverse acoustic, TA) SAW modes were coherently excited and detected in a 10-nm-thick BTO layer, exhibiting propagation distances exceeding 80 μm (Fig. 17(h)). By applying an in-plane $\boldsymbol{H}$, clear hybridization and anticrossing behavior between the SAWs and spin waves in LSMO were observed in the transmission spectra. The wavelength of the resulting MPs can be precisely tuned via the $\boldsymbol{H}$ strength and orientation relative to the acoustic wave vector (Figs. 17(i)–17(l)). A theoretical model incorporating effective interlayer MEC successfully reproduces the experimental spectra, yielding an estimated coupling strength on the order of 2×10^5 J/m^3 (Figs. 17(m) and 17(n)). These results not only reveal the long-range phase-coherent nature of magnon-polaron dynamics but also highlight the potential of using ferroelectric thin films for guiding and electrically controlling hybrid magnonic excitations in integrated spintronic and magnonic devices.

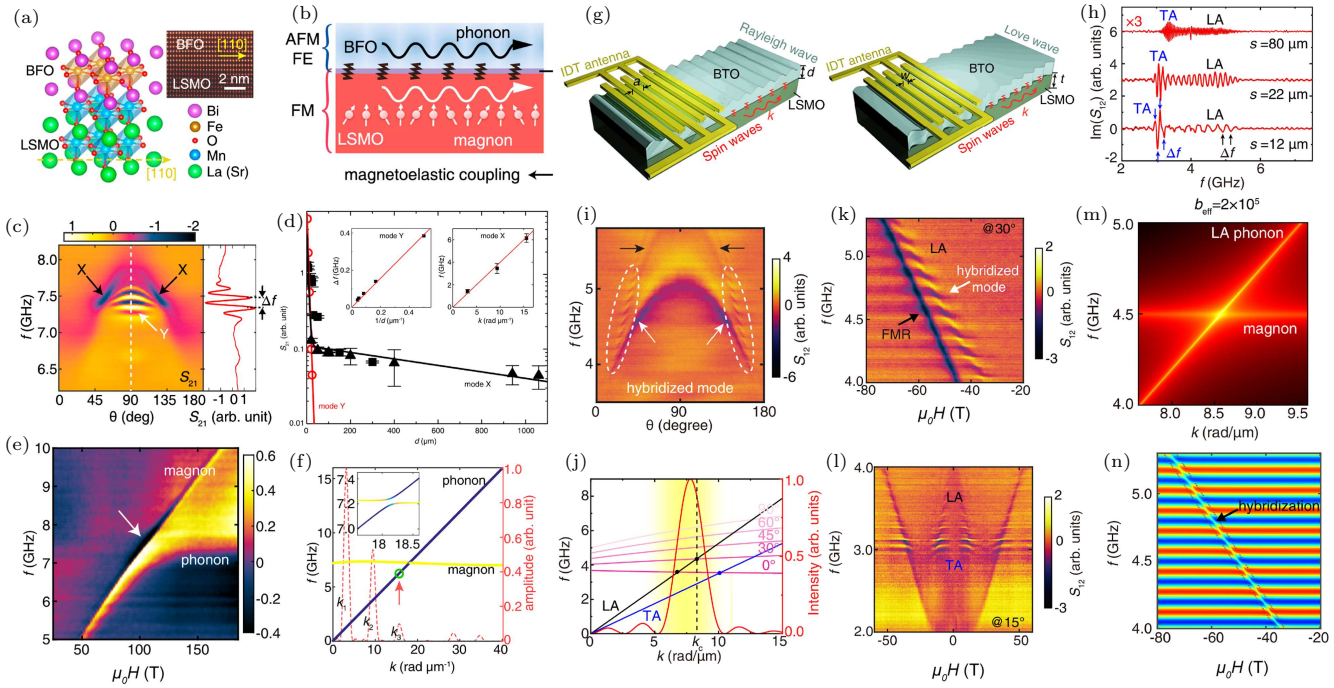


Fig. 17. Schematic diagrams of the interface (a) and magnon–phonon coupling (b) in the BFO/LSMO heterostructure. Spin-wave transmission spectra (c) and amplitude as a function of the distance d between excitation and detection antennas (d) for modes X and Y. An anticrossing-like feature induced by magnon–phonon coupling in measurements (e) and simulation results (f). Reprinted with permission from Ref. [78]. Copyright 2021 by Springer Nature. (g) Diagram illustrating the excitation of Rayleigh and Love SAWs. (h) SAWs transmission spectra of TA and LA modes obtained at different propagation distances without $\boldsymbol{H}$. (i) θ-dependent transmission spectra of SAWs. (j) Dispersion of the LA, TA modes, and spin waves at different θ between the k and $\boldsymbol{H}$. $\boldsymbol{H}$ dependence of transmission spectra at $\theta = 30°$ (k) and 15° (l). Hybridized dispersion of spin waves and LA mode (m) and calculated transmission spectra (n). Reprinted with permission from Ref. [79]. Copyright 2023 by American Physical Society.

5. Summary and outlook

This review has synthesized the rapid advancements in the field of MPs, tracing their development from fundamental MEC concepts to their manifestation as distinct hybrid quasiparticles in complex material systems. We have detailed the comprehensive toolkit now available for probing these excitations, ranging from the spectral precision of inelastic neutron and light scattering to the sensitive transport measurements provided by spin pumping and spin caloritronic effects (SSE and SPE).

Crucially, the study of MPs has shifted the paradigm regarding phonon–magnon interactions. Rather than viewing lattice vibrations merely as a source of damping or dissipation, it is now evident that strong MEC can be harnessed to engineer hybrid states with superior transport properties. The formation of MPs fundamentally alters the landscape of spin and heat transport, serving as the physical mechanism underpinning anomalies in the SSE and facilitating the long-distance propagation of spin information. This coupling has effectively laid the foundation for acoustic spintronics, enabling the coherent interconversion of information between spin and lattice degrees of freedom.

Looking forward, the field is poised to transition from fundamental characterization to active quantum control and device integration. We identify several compelling directions that will likely define the next era of magnon-polaron research.

Altermagnetism The recently emerged class of altermagnets offers a novel platform for magnonics.[207] Unlike conventional antiferromagnets, altermagnets are predicted to host highly anisotropic, momentum-dependent magnon bands with significant chiral splitting.[138,208–214] Investigating MPs within this regime could unlock robust, high-frequency information carriers that leverage the unique symmetry of altermagnetic order for enhanced lifetime and control.[215]

Ultrafast and non-equilibrium dynamics Moving beyond static control, the use of femtosecond optical and terahertz pulses to manipulate MPs offers a pathway to ultrafast information processing.[216] Real-time tracking of magnon-polaron formation and decoherence will be critical for developing optical switching protocols that operate on the timescale of the lattice dynamics.

Topological magnon polarons The interplay between MPs and magnetic topology represents a rich frontier.[52,217–220] Non-collinear magnetic textures, such as skyrmions and spin spirals,[181] provide a symmetry-breaking landscape ideal for engineering topologically protected MP states.[220] Future efforts should focus on tailoring these states in van der Waals magnets and heterostructures to realize dissipationless chiral edge currents, which are essential for low-loss magnonic logic.[218,221]

Potential directions in quantum information processing The coherent hybrid nature of magnon polarons makes them ideal quantum transducers, where long-lived phonons could serve as quantum memories for magnonic states or facilitate microwave-to-optical conversion for quantum networks.[222–228] The recent prediction of topological phases in magnon polarons opens possibilities for engineering robust, decoherence-protected edge channels as quantum information pathways.[217–220] The strong nonlinearities in magnon systems, mediated by phonons, may also enable the generation of macroscopic quantum states, with applications in quantum metrology.

In conclusion, the evolution of magnon polarons from a theoretical concept to a cornerstone of modern condensed matter physics exemplifies the power of correlated dynamics in solids. By mastering the entanglement between spin and lattice, the community is charting a clear course toward a new generation of energy-efficient, coherent, and multifunctional information technologies.

Acknowledgements

This work was supported by the National Key Research and Development Program of China (Grant No. 2025YFA1411100), the National Natural Science Foundation of China (Grant Nos. U24A6002 (X. Xu), 12374118 (Z. Shi), 52171183 (Z. Quan), 12274322 (Y. Liu), 52471254(Y. Liu), 12174287(J. Zhang), and 12504143 (Y. Li)). Z. Shi acknowledges the support from the Natural Science Foundation of Shanghai (Grant No. 23ZR1466800). Y. Li acknowledges the support from the Basic Research Plan of Shanxi Province (Grant No. 202503021212212).

References

[1] Bloch V F 1930 *Z. Phys.* **61** 206
[2] J.Frenkel 1933 *Nature* **131** 860
[3] Dyson F J 1956 *Phys. Rev.* **102** 1217
[4] Prabhakar A and Stancil D 2009 *Spin Waves: Theory and Applications* (Springer)
[5] Kajiwara Y, Harii K, Takahashi S, Ohe J, Uchida K, Mizuguchi M, Umezawa H, Kawai H, Ando K, Takanashi K, Maekawa S and Saitoh E 2010 *Nature* **464** 262
[6] Brockhouse B N 1957 *Phys. Rev.* **106** 859
[7] Gurevich A G and Melkov G A 1996 *Magnetization Oscillations and Waves* (CRC Press)
[8] Chumak A V, Vasyuchka. V I, Serga A A and Hillebrands B 2015 *Nat. Phys.* **11** 453
[9] Chumak A V, Serga A A and Hillebrands B 2014 *Nat. Commun.* **5** 4700
[10] Cramer J, Fuhrmann F, Ritzmann U, Gall V, Niizeki T, Ramos R, Qiu Z, Hou D, Kikkawa T, Sinova J, Nowak U, Saitoh E and Kläui M 2018 *Nat. Commun.* **9** 1089
[11] Guo C Y, Wan C H, Wang X, Fang C, Tang P, Kong W J, Zhao M K, Jiang L N, Tao B S, Yu G Q and Han X F 2018 *Phys. Rev. B* **98** 134426
[12] Wu H, Huang L, Fang C, Yang B S, Wan C H, Yu G Q, Feng J F, Wei H X and Han X F 2018 *Phys. Rev. Lett.* **120** 097205
[13] Chen P, Chi B, Wang H, Zhang D, Xia J, Dong J, He W, Wang Y, Guo T, Chen P, Liu Y, Yu H, Yu G, Wan C and Han X 2024 *Phys. Rev. Appl.* **22** 054023
[14] Cheng J, Yu R, Sun L, He K, Ji T, Yang M, Zhang Z, Hu X, Niu H, Yang X, Chen P, Chen G, Xiao J, Huang F, Lu X, Cai H, Yuan H, Miao B and Ding H 2024 *Nat. Commun.* **15** 9314
[15] Han X, Wu H and Zhang T 2024 *Appl. Phys. Lett.* **125** 020501

[16] Wang F, Shi G, Yang D, Tan H R, Zhang C, Lei J, Pu Y, Yang S, Soumyanarayanan A, Elyasi M and Yang H 2024 *Nat. Nanotechnol.* **19** 1478
[17] Wang Y Z, Zhang T Y, Dong J, Chen P, Yu G Q, Wan C H and Han X F 2024 *Phys. Rev. Lett.* **132** 076701
[18] Yang D, Kim T, Lee K, Xu C, Liu Y, Wang F, Zhao S, Kumar D and Yang H 2024 *Nat. Commun.* **15** 4046
[19] Wang Y, Zhu D, Yang Y, Lee K, Mishra R, Go G, Oh S H, Kim D H, Cai K, Liu E, Pollard S D, Shi S, Lee J, Teo K L, Wu Y, Lee K J and Yang H 2019 *Science* **366** 1125
[20] Zhou Y, Guo T, Han L, Liao L, He W, Wan C, Chen C, Wang Q, Qiao L, Bai H, Zhu W, Zhang Y, Chen R, Han X, Pan F and Song C 2024 *Sci. Adv.* **10** eadk7935
[21] Li K, Wang L, Wang Y, Guo Y, Lv S, He Y, Lin W, Min T, Hu S, Yang S, Xue D, Zheng A, Yang S and Ding X 2024 *Adv. Mater.* **36** 2312137
[22] Huang X, Chen X, Li Y, Mangeri J, Zhang H, Ramesh M, Taghinejad H, Meisenheimer P, Caretta L, Susarla S, Jain R, Klewe C, Wang T, Chen R, Hsu C H, Harris I, Husain S, Pan H, Yin J, Shafer P, Qiu Z, Rodrigues D R, Heinonen O, Vasudevan D, Íñiguez J, Schlom D G, Salahuddin S, Martin L W, Analytis J G, Ralph D C, Cheng R, Yao Z and Ramesh R 2024 *Nat. Mater.* **23** 898
[23] Chai Y, Liang Y, Xiao C, Wang Y, Li B, Jiang D, Pal P, Tang Y, Chen H, Zhang Y, Bai H, Xu T, Jiang W, Skowroński W, Zhang Q, Gu L, Ma J, Yu P, Tang J, Lin Y H, Yi D, Ralph D C, Eom C B, Wu H and Nan T 2024 *Nat. Commun.* **15** 5975
[24] Schneider T, Serga A A, Leven B, Hillebrands B, Stamps R L and Kostylev M P 2008 *Appl. Phys. Lett.* **92** 022505
[25] Born M and Huang K 1996 *Dynamical Theory Of Crystal Lattices* (New York: Oxford Academic)
[26] Abrahams E and Kittel C 1952 *Phys. Rev.* **88** 1200
[27] Kittel C and Abrahams E 1953 *Rev. Mod. Phys.* **25** 233
[28] Godejohann F, Scherbakov A V, Kukhtaruk S M, Poddubny A N, Yaremkevich D D, Wang M, Nadzeyka A, Yakovlev D R, Rushforth A W, Akimov A V and Bayer M 2020 *Phys. Rev. B* **102** 144438
[29] Hashimoto Y, Bossini D, Johansen T H, Saitoh E, Kirilyuk A and Rasing T 2018 *Phys. Rev. B* **97** 140404
[30] Guerreiro S C and Rezende S M 2015 *Phys. Rev. B* **92** 214437
[31] Kobayashi T, Barker R C, Bleustein J L and Yelon A 1973 *Phys. Rev. B* **7** 3273
[32] Brown W F 1965 *J. Appl. Phys.* **36** 994
[33] Callen E R and Callen H B 1963 *Phys. Rev.* **129** 578
[34] Rückriegel A, Kopietz P, Bozhko D A, Serga A A and Hillebrands B 2014 *Phys. Rev. B* **89** 184413
[35] Kikkawa T, Shen K, Flebus B, Duine R A, Uchida K, Qiu Z, Bauer G E W and Saitoh E 2016 *Phys. Rev. Lett.* **117** 207203
[36] Cornelissen L J, Oyanagi K, Kikkawa T, Qiu Z, Kuschel T, Bauer G E W, van Wees B J and Saitoh E 2017 *Phys. Rev. B* **96** 104441
[37] Flebus B, Shen K, Kikkawa T, Uchida K, Qiu Z, Saitoh E, Duine R A and Bauer G E W 2017 *Phys. Rev. B* **95** 144420
[38] Ramos R, Hioki T, Hashimoto Y, Kikkawa T, Frey P, Kreil A J E, Vasyuchka V I, Serga A A, Hillebrands B and Saitoh E 2019 *Nat. Commun.* **10** 5162
[39] Oh J, Le M D, Nahm H H, Sim H, Jeong J, Perring T G, Woo H, Nakajima K, Ohira-Kawamura S, Yamani Z, Yoshida Y, Eisaki H, Cheong S W, Chernyshev A L and Park J G 2016 *Nat. Commun.* **7** 13146
[40] Brown W F 1966 *Magnetoelastic Interactions* (New York: Springer-Verlag)
[41] Bauer G E W, Saitoh E and van Wees B J 2012 *Nat. Mater.* **11** 391
[42] Schmidt R and Brouwer P W 2021 *Phys. Rev. B* **103** 014412
[43] Harris A B 1963 *Phys. Rev.* **132** 2398
[44] Srivastava C M and Aiyar R 1987 *J. Phys. C: Solid St. Phys.* **20** 1119
[45] Cherepanov V, Kolokolov I and L'vov V 1993 *Phys. Rep.-Rev. Sec. Phys. Lett.* **229** 81
[46] Kittel C 1958 *Phys. Rev.* **110** 836
[47] Rückriegel A, Streib S, Bauer G E W and Duine R A 2020 *Phys. Rev. B* **101** 104402
[48] Rückriegel A and Duine R A 2020 *Phys. Rev. Lett.* **124** 117201
[49] Kamra A, Keshtgar H, Yan P and Bauer G E W 2015 *Phys. Rev. B* **91** 104409
[50] Shi Z, Xi Q, Li J, Li Y, Aldosary M, Xu Y, Zhou J, Zhou S M and Shi J 2021 *Phys. Rev. Lett.* **127** 277203
[51] Man H, Shi Z, Xu G, Xu Y, Chen X, Sullivan S, Zhou J, Xia K, Shi J and Dai P 2017 *Phys. Rev. B* **96** 100406
[52] Bao S, Gu Z L, Shangguan Y, Huang Z, Liao J, Zhao X, Zhang B, Dong Z Y, Wang W, Kajimoto R, Nakamura M, Fennell T, Yu S L, Li J X and Wen J 2023 *Nat. Commun.* **14** 6093
[53] Holanda J, Maior D S, Azevedo A and Rezende S M 2018 *Nat. Phys.* **14** 500
[54] Hashimoto Y, Daimon S, Iguchi R, Oikawa Y, Shen K, Sato K, Bossini D, Tabuchi Y, Satoh T, Hillebrands B, Bauer G E W, Johansen T H, Kirilyuk A, Rasing T and Saitoh E 2017 *Nat. Commun.* **8** 15859
[55] Bozhko D A, Clausen P, Melkov G A, L'vov V S, Pomyalov A, Vasyuchka V I, Chumak A V, Hillebrands B and Serga A A 2017 *Phys. Rev. Lett.* **118** 237201
[56] Lai J M, Xie Y R and Zhang J 2020 *Nano Res.* **14** 1711
[57] Liu S, Granados del Águila A, Bhowmick D, Gan C K, Thu Ha Do T, Prosnikov M A, Sedmidubský D, Sofer Z, Christianen P C M, Sengupta P and Xiong Q 2021 *Phys. Rev. Lett.* **127** 097401
[58] Mai T T, Garrity K F, McCreary A, Argo J, Simpson J R, Doan-Nguyen V, Aguilar R V and Walker A R H 2021 *Sci. Adv.* **7** eabj3106
[59] Sun Y J, Pang S M and Zhang J 2021 *Chin. Phys. B* **30** 117104
[60] Cui J, Boström E V, Ozerov M, Wu F, Jiang Q, Chu J H, Li C, Liu F, Xu X, Rubio A and Zhang Q 2023 *Nat. Commun.* **14** 3396
[61] Hu L, Du K Z, Chen Y, Zhai Y, Wang X and Xiong Q 2023 *Natl. Sci. Open* **2** 20230002
[62] Wang Z N, Lv Y P, Chang H N and Jun Z 2025 *Chin. Phys. B* **34** 107201
[63] Agrawal M, Vasyuchka V I, Serga A A, Karenowska A D, Melkov G A and Hillebrands B 2013 *Phys. Rev. Lett.* **111** 107204
[64] An K, Olsson K S, Weathers A, Sullivan S, Chen X, Li X, Marshall L G, Ma X, Klimovich N, Zhou J, Shi L and Li X 2016 *Phys. Rev. Lett.* **117** 107202
[65] Olsson K S, An K, Fiete G A, Zhou J, Shi L and Li X 2020 *Phys. Rev. X* **10** 021029
[66] Hayashi H and Ando K 2018 *Phys. Rev. Lett.* **121** 237202
[67] Kikkawa T and Saitoh E 2022 *Annu. Rev. Condens. Matter Phys.* **14** 129
[68] Shen K 2019 *Phys. Rev. B* **99** 024417
[69] Li J, Simensen H T, Reitz D, Sun Q, Yuan W, Li C, Tserkovnyak Y, Brataas A and Shi J 2020 *Phys. Rev. Lett.* **125** 217201
[70] Xing W, Ma Y, Yao Y, Cai R, Ji Y, Xiong R, Shen K and Han W 2020 *Phys. Rev. B* **102** 184416
[71] Yang B, Xia S Y, Zhao H, Liu G, Du J, Shen K, Qiu Z and Wu D 2021 *Phys. Rev. B* **103** 054411
[72] Kikkawa T, Oyanagi K, Hioki T, Ishida M, Qiu Z, Ramos R, Hashimoto Y and Saitoh E 2022 *Phys. Rev. Mater.* **6** 104402
[73] Li Y, Duan Y, Wang M, Lang L, Zhang Y, Yang M, Li J, Fan W, Shen K, Shi Z and Zhou S-M 2024 *Phys. Rev. Lett.* **132** 056702
[74] Wang H, Hou D, Kikkawa T, Ramos R, Shen K, Qiu Z, Chen Y, Umeda M, Shiomi Y, Jin X and Saitoh E 2018 *Appl. Phys. Lett.* **112** 142406
[75] Li Y, Duan Y, Wang M, Lang L, Zhang Y, Shen K, Shi Z and Zhou S-M 2025 *npj Spintronics* **3** 15
[76] Yahiro R, Kikkawa T, Ramos R, Oyanagi K, Hioki T, Daimon S and Saitoh E 2020 *Phys. Rev. B* **101** 024407
[77] Weiler M, Dreher L, Heeg C, Huebl H, Gross R, Brandt M S and Goennenwein S T B 2011 *Phys. Rev. Lett.* **106** 117601
[78] Zhang J, Chen M, Chen J, Yamamoto K, Wang H, Hamdi M, Sun Y, Wagner K, He W, Zhang Y, Ma J, Gao P, Han X, Yu D, Maletinsky P, Ansermet J-P, Maekawa S, Grundler D, Nan C-W and Yu H 2021 *Nat. Commun.* **12** 7258
[79] Wang H, Yang Y, Chen J, Wang J, Jia H, Chen P, Zhang Y, Wan C, Liu S, Yu D, Han X, Ansermet J P, Zhang J and Yu H 2023 *Phys. Rev. B* **108** 144425
[80] Kittel C 1948 *Phys. Rev.* **73** 155
[81] Vaidya P, Morley S A, Tol J v, Liu Y, Cheng R, Brataas A, Lederman D and Barco E d 2020 *Science* **368** 160
[82] Li J, Wilson C B, Cheng R, Lohmann M, Kavand M, Yuan W, Aldosary M, Agladze N, Wei P, Sherwin M S and Shi J 2020 *Nature* **578** 70
[83] Han J, Zhang P, Bi Z, Fan Y, Safi T S, Xiang J, Finley J, Fu L, Cheng R and Liu L 2020 *Nat. Nanotechnol.* **15** 563
[84] Cheng R, Xiao J, Niu Q and Brataas A 2014 *Phys. Rev. Lett.* **113** 057601
[85] Hattori T, Fukuoka A, Kawagita K, Tada K, Ishikawa Y, Yamaguchi Y, Tatematsu Y, Fujii Y, Kimata M, Kimura S, Kan D, Ohe J and Moriyama T 2024 *Phys. Rev. Lett.* **133** 256701
[86] Chen X, Zheng C and Liu Y 2024 *Magnetochemistry* **10** 50
[87] Chen X, Zheng C, Zhou S, Liu Y and Zhang Z 2021 *Magnetochemistry* **8** 7

[88] Chen X, Zheng C, Zhang Y, Zhou S, Liu Y and Zhang Z 2021 *New J. Phys.* **23** 113029

[89] Chen X, Zheng C, Zhou S, Liu Y and Zhang Z 2021 *J. Phys. Condens. Matter* **34** 015802

[90] Zhang Z, Gao F Y, Curtis J B, Liu Z J, Chien Y C, von Hoegen A, Wong M T, Kurihara T, Suemoto T, Narang P, Baldini E and Nelson K A 2024 *Nat. Phys.* **20** 801

[91] Zhang Z, Gao F Y, Chien Y C, Liu Z J, Curtis J B, Sung E R, Ma X, Ren W, Cao S, Narang P, von Hoegen A, Baldini E and Nelson K A 2024 *Nat. Phys.* **20** 788

[92] Shiota Y, Taniguchi T, Hayashi D, Narita H, Karube S, Hisatomi R, Moriyama T and Ono T 2024 *Nat. Commun.* **15** 9750

[93] Leenders R A, Afanasiev D, Kimel A V and Mikhaylovskiy R V 2024 *Nature* **630** 335

[94] Kim C, Lee S, Kim H G, Park J H, Moon K W, Park J Y, Yuk J M, Lee K J, Park B G, Kim S K, Kim K J and Hwang C 2020 *Nat. Mater.* **19** 980

[95] Wang L, Shen L, Bai H, Zhou H A, Shen K and Jiang W 2024 *Phys. Rev. Lett.* **133** 166705

[96] Finley J and Liu L 2020 *Appl. Phys. Lett.* **116** 110501

[97] Liensberger L, Kamra A, Maier-Flaig H, Geprags S, Erb A, Goennenwein S T B, Gross R, Belzig W, Huebl H and Weiler M 2019 *Phys. Rev. Lett.* **123** 117204

[98] Liu Y, Xu Z, Liu L, Zhang K, Meng Y, Sun Y, Gao P, Zhao H W, Niu Q and Li J 2022 *Nat. Commun.* **13** 1264

[99] Kim S K, Beach G S D, Lee K-J, Ono T, Rasing T and Yang H 2021 *Nat. Mater.* **21** 24

[100] Li Y, Wang W, Liu C, Chen A, Zheng D, Yang T, Tang M, Fang B, Ma Y, Shen K, Manchon A, Qiu Z and Zhang X 2025 *Adv. Mater.* **37** 2416190

[101] Duan Y, Cong A and Shen K 2025 *Phys. Rev. Appl.* **23** L051006

[102] Serga A A, Chumak A V and Hillebrands B 2010 *J. Phys. D: Appl. Phys.* **43** 264002

[103] Geller S and Gilleo M A 1957 *Acta Crystallogr.* **10** 239

[104] Wesenberg D, Liu T, Balzar D, Wu M and Zink B L 2017 *Nat. Phys.* **13** 987

[105] Cornelissen L J, Liu J, Duine R A, Youssef J B and van Wees B J 2015 *Nat. Phys.* **11** 1022

[106] Gilleo M A and Geller S 1958 *Phys. Rev.* **110** 73

[107] Sun Y and Wu M 2013 *Solid State Phys.* **64** 157

[108] Dionne G F 2009 *Magnetic Oxides* (Springer)

[109] Nambu Y, Barker J, Okino Y, Kikkawa T, Shiomi Y, Enderle M, Weber T, Winn B, Graves-Brook M, Tranquada J M, Ziman T, Fujita M, Bauer G E W, Saitoh E and Kakurai K 2020 *Phys. Rev. Lett.* **125** 027201

[110] Shen K 2018 *New J. Phys.* **20** 043025

[111] Fleury P A and Loudon R 1968 *Phys. Rev.* **166** 514

[112] Peter Y Yu and Cardona M 2010 *Fundamentals of Semiconductors* (Springer)

[113] Wang Y, Guo M and Wang Q 2025 *Acta Phys. Sin.* **74** 237201 (in Chinese)

[114] Luo J, Li S, Ye Z, Xu R, Yan H, Zhang J, Ye G, Chen L, Hu D, Teng X, Smith W A, Yakobson B I, Dai P, Nevidomskyy A H, He R and Zhu H 2023 *Nano Lett.* **23** 2023

[115] Sun Y J, Lai J M, Pang S M, Liu X L, Tan P H and Zhang J 2022 *J. Phys. Chem. Lett.* **13** 1533

[116] Sun Y, Liu B, Gan C K, Xia S, Lin H, Liu S and Yu T 2025 *Nanoscale* **17** 8476

[117] Tserkovnyak Y, Brataas A and Bauer G E W 2002 *Phys. Rev. Lett.* **88** 117601

[118] Costache M V, Sladkov M, Watts S M, van der Wal C H and van Wees B J 2006 *Phys. Rev. Lett.* **97** 216603

[119] Mosendz O, Pearson J E, Fradin F Y, Bauer G E W, Bader S D and Hoffmann A 2010 *Phys. Rev. Lett.* **104** 046601

[120] Heinrich B, Burrowes C, Montoya E, Kardasz B, Girt E, Song Y Y, Sun Y and Wu M 2011 *Phys. Rev. Lett.* **107** 066604

[121] Sun Y, Chang H, Kabatek M, Song Y Y, Wang Z, Jantz M, Schneider W, Wu M, Montoya E, Kardasz B, Heinrich B, te Velthuis S G E, Schultheiss H and Hoffmann A 2013 *Phys. Rev. Lett.* **111** 106601

[122] Weiler M, Althammer M, Schreier M, Lotze J, Pernpeintner M, Meyer S, Huebl H, Gross R, Kamra A, Xiao J, Chen Y T, Jiao H, Bauer G E W and Goennenwein S T B 2013 *Phys. Rev. Lett.* **111** 176601

[123] Lee T, Park M T, Ko H W, Oh J H, Ko S, Hwang S, Jang J G, Baek G W, Kim S K, Lee H W, Jung M H, Kim K J and Lee K J 2025 *Nature* **638** 106

[124] Sandweg C W, Kajiwara Y, Chumak A V, Serga A A, Vasyuchka V I, Jungfleisch M B, Saitoh E and Hillebrands B 2011 *Phys. Rev. Lett.* **106** 216601

[125] Uchida K, Takahashi S, Harii K, Ieda J, Koshibae W, Ando K, Maekawa S and Saitoh E 2008 *Nature* **455** 778

[126] Jaworski C M, Yang J, Mack S, Awschalom D D, Heremans J P and Myers R C 2010 *Nat. Mater.* **9** 898

[127] Uchida K, Xiao J, Adachi H, Ohe J, Takahashi S, Ieda J, Ota T, Kajiwara Y, Umezawa H, Kawai H, Bauer G E, Maekawa S and Saitoh E 2010 *Nat. Mater.* **9** 894

[128] Uchida K, Adachi H, Ota T, Nakayama H, Maekawa S and Saitoh E 2010 *Appl. Phys. Lett.* **97** 172505

[129] Seki S, Ideue T, Kubota M, Kozuka Y, Takagi R, Nakamura M, Kaneko Y, Kawasaki M and Tokura Y 2015 *Phys. Rev. Lett.* **115** 266601

[130] Wu S M, Zhang W, Kc A, Borisov P, Pearson J E, Jiang J S, Lederman D, Hoffmann A and Bhattacharya A 2016 *Phys. Rev. Lett.* **116** 097204

[131] Li J, Shi Z, Ortiz V H, Aldosary M, Chen C, Aji V, Wei P and Shi J 2019 *Phys. Rev. Lett.* **122** 217204

[132] Xing W, Qiu L, Wang X, Yao Y, Ma Y, Cai R, Jia S, Xie X C and Han W 2019 *Phys. Rev. X* **9** 011026

[133] He X, Ding S, Giil H G, Wang J, Bhukta M, Wu M, Shi W, Lin Z, Liang Z, Yang J, Kläui M, Brataas A, Hou Y and Wu R 2025 *Nat. Commun.* **16** 3037

[134] Chen G, Qi S, Liu J, Chen D, Wang J, Yan S, Zhang Y, Cao S, Lu M, Tian S, Chen K, Yu P, Liu Z, Xie X C, Xiao J, Shindou R and Chen J H 2021 *Nat. Commun.* **12** 6279

[135] Ghiasi T S, Kaverzin A A, Dismukes A H, de Wal D K, Roy X and van Wees B J 2021 *Nat. Nanotechnol.* **16** 788

[136] Wu S M, Pearson J E and Bhattacharya A 2015 *Phys. Rev. Lett.* **114** 186602

[137] Oyanagi K, Takahashi S, Kikkawa T and Saitoh E 2023 *Phys. Rev. B* **107** 014423

[138] Cui Q, Zeng B, Cui P, Yu T and Yang H 2023 *Phys. Rev. B* **108** L180401

[139] Ullah A, Bezzerga D and Hong J 2024 *Mater. Today Phys.* **47** 101539

[140] Ashani T M, Ashani A and Hong J 2025 *Energy Mater.* **5** 500111

[141] Weißenhofer M and Marmodoro A 2024 *Phys. Rev. B* **110** 094427

[142] Uchida K, Adachi H, Kikkawa T, Kirihara A, Ishida M, Yorozu S, Maekawa S and Saitoh E 2016 *Proc. IEEE* **104** 1946

[143] Qiu Z, Hou D, Barker J, Yamamoto K, Gomonay O and Saitoh E 2018 *Nat. Mater.* **17** 577

[144] Yuan W, Li J and Shi J 2020 *Appl. Phys. Lett.* **117** 100501

[145] Cramer J, Guo E J, Geprags S, Kehlberger A, Ivanov Y P, Ganzhorn K, Della Coletta F, Althammer M, Huebl H, Gross R, Kosel J, Klaui M and Goennenwein S T B 2017 *Nano Lett.* **17** 3334

[146] Geprägs S, Kehlberger A, Coletta F D, Qiu Z, Guo E J, Schulz T, Mix C, Meyer S, Kamra A, Althammer M, Huebl H, Jakob G, Ohnuma Y, Adachi H, Barker J, Maekawa S, Bauer G E W, Saitoh E, Gross R, Goennenwein S T B and Klaui M 2016 *Nat. Commun.* **7** 10452

[147] Gu Y, Barker J, Li J, Kikkawa T, Camino F, Kisslinger K, Sinsheimer J, Lienhard L, Bauer J J, Ross C A, Basov D N, Saitoh E, Pelliciari J, Bauer G E W and Bisogni V 2025 *Nature* **645** 900

[148] Flipse J, Dejene F K, Wagenaar D, Bauer G E W, Youssef J B and van Wees B J 2014 *Phys. Rev. Lett.* **113** 027601

[149] Daimon S, Iguchi R, Hioki T, Saitoh E and Uchida K I 2016 *Nat. Commun.* **7** 13754

[150] Hansen P, Witter K and Tolksdorf W 1983 *Phys. Rev. B* **27** 6608

[151] Hansen P and Krumme J P 1984 *Thin Solid Films* **114** 69

[152] Kumar R, Samantaray B and Hossain Z 2019 *J. Phys.: Condens. Matter* **31** 435802

[153] Barker J and Bauer G E W 2016 *Phys. Rev. Lett.* **117** 217201

[154] Xie L S, Jin G X, He L, Bauer G E W and Xia K 2017 *Phys. Rev. B* **95** 014423

[155] Liu Y, Xie L S, Yuan Z and Xia K 2017 *Phys. Rev. B* **96** 174416

[156] Li Y, Zheng D, Fang B, Liu C, Zhang C, Chen A, Ma Y, Shen K, Liu H, Manchon A and Zhang X 2022 *Adv. Mater.* **34** e2200019

[157] Li Y, Zhang Z, Liu C, Zheng D, Fang B, Zhang C, Chen A, Ma Y, Wang C, Liu H, Shen K, Manchon A, Xiao J Q, Qiu Z, Hu C M and Zhang X 2024 *Nat. Commun.* **15** 2234

[158] Kikkawa T, Uchida K, Daimon S, Qiu Z, Shiomi Y and Saitoh E 2015 *Phys. Rev. B* **92** 064413

[159] Comstock R L, Raymond J J, Nilsen W G and Remeika J P 1966 *Appl. Phys. Lett.* **9** 274

[160] Tomasello B, Mannix D, Geprägs S and Ziman T 2022 *Ann. Phys.* **447** 169117
[161] Lahoubi M, Guillot M, Marchand A, Tcheou F and Roudault E 1984 *IEEE Trans. Magn.* **20** 1518
[162] Guillot M, Tcheou F, Marchand A and Feldmann P 1984 *Z. Phys. B* **56** 29
[163] Pickart S J, Alperin H A and Clark A E 1970 *J. Appl. Phys.* **41** 1192
[164] Guillot M, Marchand A, Tchéou F and Feldmann P 1982 *J. Appl. Phys.* **53** 2719
[165] Lahoubi M 2012 *J. Phys. Conf. Ser.* **340** 012068
[166] Bouguerra A, Fillion G, de Brion S, Khène S, Wolfers P and Hlil E K 2008 *J. Phys. Condens. Matter* **20** 295231
[167] Vien T K and Dorman J L 1977 *Phys. Lett.* **61A** 336
[168] Mori M, Tomasello B and Ziman T 2025 *Phys. Rev. B* **111** 014407
[169] Kubota M, Tsukazaki A, Kagawa F, Shibuya K, Tokunaga Y, Kawasaki M and Tokura Y 2012 *Appl. Phys. Express* **5** 103002
[170] Wang L W, Xie L S, Xu P X and Xia K 2020 *Phys. Rev. B* **101** 165137
[171] Kawamoto Y, Kikkawa T, Kawamata M, Umemoto Y, Manning A G, Rule K C, Ikeuchi K, Kamazawa K, Fujita M, Saitoh E, Kakurai K and Nambu Y 2024 *Appl. Phys. Lett.* **124** 132406
[172] Li Y, Yang X, Bai H, Wang M, Cheng D, Song C, Yuan Z, Liu Y and Shi Z 2023 *Phys. Rev. B* **108** 184403
[173] Liang J M, Zhao X W, Liu Y K, Li P G, Ng S M, Wong H F, Cheng W F, Zhou Y, Dai J Y, Mak C L and Leung C W 2023 *Appl. Phys. Lett.* **122** 242401
[174] Li P G, Liang J M, Ng S M, Wong H F, Zhou Y, Huang L J, Lin K W, Tsang Y H, Mak C L and Leung C W 2024 *J. Magn. Magn. Mater.* **592** 171785
[175] Schlauderer S, Lange C, Baierl S, Ebnet T, Schmid C P, Valovcin D C, Zvezdin A K, Kimel A V, Mikhaylovskiy R V and Huber R 2019 *Nature* **569** 383
[176] Hortensius J R, Afanasiev D, Matthiesen M, Leenders R, Citro R, Kimel A V, Mikhaylovskiy R V, Ivanov B A and Caviglia A D 2021 *Nat. Phys.* **17** 1001
[177] Baltz V, Manchon A, Tsoi M, Moriyama T, Ono T and Tserkovnyak Y 2018 *Rev. Mod. Phys.* **90** 015005
[178] Kampfrath T, Sell A, Klatt G, Pashkin A, Mährlein S, Dekorsy T, Wolf M, Fiebig M, Leitenstorfer A and Huber R 2010 *Nat. Photonics* **5** 31
[179] Gomonay O, Baltz V, Brataas A and Tserkovnyak Y 2018 *Nat. Phys.* **14** 213
[180] Wang H, Yuan R, Zhou Y, Zhang Y, Chen J, Liu S, Jia H, Yu D, Ansermet J P, Song C and Yu H 2023 *Phys. Rev. Lett.* **130** 096701
[181] Zhang Y, Qiu L, Chen J, Wu S, Wang H, Malik I A, Cai M, Wu M, Gao P, Hua C, Yu W, Xiao J, Jiang Y, Yu H, Shen K and Zhang J 2025 *Nat. Mater.* **24** 69
[182] Sheng L, Duvakina A, Wang H, Yamamoto K, Yuan R, Wang J, Chen P, He W, Yu K, Zhang Y, Chen J, Hu J, Song W, Liu S, Han X, Yu D, Ansermet J-P, Maekawa S, Grundler D and Yu H 2025 *Nat. Phys.* **21** 740
[183] Ross A, Lebrun R, Evers M, Deák A, Szunyogh L, Nowak U and Kläui M 2021 *Phys. Rev. B* **103** 224433
[184] Chen X, Zheng C, Xu H and Liu Y 2025 *J. Phys. Condens. Matter* **37** 135802
[185] Zheng C, Chen X, Zhou S and Liu Y 2022 *J. Phys. Condens. Matter* **35** 085801
[186] Liu H and Shen K 2022 *J. Appl. Phys.* **131** 103902
[187] Yuan W, Zhu Q, Su T, Yao Y, Xing W, Chen Y, Ma Y, Lin X, Shi J, Shindou R, Xie X C and Han W 2018 *Sci. Adv.* **4** eaat1098
[188] Zhang Y H, Chuang T C, Qu D and Huang S Y 2022 *Phys. Rev. B* **105** 094442
[189] Yamamoto Y, Ichioka M and Adachi H 2022 *Phys. Rev. B* **105** 104417
[190] Reitz D, Li J, Yuan W, Shi J and Tserkovnyak Y 2020 *Phys. Rev. B* **102** 020408
[191] Kurumaji T, Ishiwata S and Tokura Y 2015 *Phys. Rev. X* **5** 031034
[192] Reschke S, Tsirlin A A, Khan N, Prodan L, Tsurkan V, Kézsmárki I and Deisenhofer J 2020 *Phys. Rev. B* **102** 094307
[193] Chang Y, Weng Y, Xie Y, You B, Wang J, Li L, Liu J M, Dong S and Lu C 2023 *Phys. Rev. Lett.* **131** 136701
[194] Wu J B, Wu H and Tan P H 2024 *Adv. Funct. Mater.* **34** 2312214
[195] Song F, Lv Y, Sun Y J, Pang S, Chang H, Guan S, Lai J M, Wang X J, Wu B, Hu C, Yuan Z and Zhang J 2024 *Nat. Commun.* **15** 7841
[196] Gong C and Zhang X 2019 *Science* **363** 706
[197] Du K Z, Wang X Z, Liu Y, Hu P, Utama M I B, Gan C K, Xiong Q and Kloc C 2015 *ACS Nano* **10** 1738
[198] Gong C, Li L, Li Z, Ji H, Stern A, Xia Y, Cao T, Bao W, Wang C, Wang Y, Qiu Z Q, Cava R J, Louie S G, Xia J and Zhang X 2017 *Nature* **546** 265
[199] Huang B, Clark G, Navarro-Moratalla E, Klein D R, Cheng R, Seyler K L, Zhong D, Schmidgall E, McGuire M A, Cobden D H, Yao W, Xiao D, Jarillo-Herrero P and Xu X 2017 *Nature* **546** 270
[200] Berk C, Jaris M, Yang W, Dhuey S, Cabrini S and Schmidt H 2019 *Nat. Commun.* **10** 1038
[201] Künstle K, Kunz Y, Moussa T, Lasinger K, Yamamoto K, Pirro P, Gregg J F, Kamra A and Weiler M 2025 *Nat. Commun.* **16** 10116
[202] Chen C, Ma M Y, Pan F and Song C 2024 *Acta. Phys. Sin.* **73** 058502 (in Chinese)
[203] Cao Y, Ding H, Zuo Y, Li X, Zhao Y, Li T, Lei N, Cao J, Si M, Xi L, Jia C, Xue D and Yang D 2024 *Nat. Commun.* **15** 1013
[204] Cao Y, Li T, Lei N, Liao L, Cui B, Xi L, Wei D, Yu T, Otani Y, Xue D and Yang D 2025 *Phys. Rev. Lett.* **135** 246705
[205] Dreher L, Weiler M, Pernpeintner M, Huebl H, Gross R, Brandt M S and Goennenwein S T B 2012 *Phys. Rev. B* **86** 134415
[206] Weiler M, Huebl H, Goerg F S, Czeschka F D, Gross R and Goennenwein S T B 2012 *Phys. Rev. Lett.* **108** 176601
[207] Song C, Bai H, Zhou Z, Han L, Reichlova H, Dil J H, Liu J, Chen X and Pan F 2025 *Nat. Rev. Mater.* **10** 473
[208] Chen X, Liu Y, Liu P, Yu Y, Ren J, Li J, Zhang A and Liu Q 2025 *Nature* **640** 349
[209] Liu Z, Ozeki M, Asai S, Itoh S and Masuda T 2024 *Phys. Rev. Lett.* **133** 156702
[210] Šmejkal L, Marmodoro A, Ahn K-H, González-Hernández R, Turek I, Mankovsky S, Ebert H, D'Souza S W, Šipr O, Sinova J and Jungwirth T 2023 *Phys. Rev. Lett.* **131** 256703
[211] Beida W, Şaşıoğlu E, Friedrich C, Bihlmayer G, Mokrousov Y and Blügel S 2025 *npj Quantum Mater.* **10** 97
[212] Sun Q, Guo J, Wang D, Abernathy D L, Tian W and Li C 2025 *Phys. Rev. Lett.* **135** 186703
[213] Wu K, Dong J, Zhu M, Zheng F and Zhang J 2025 *Chin. Phys. Lett.* **42** 070702
[214] Jin Z, Zeng Z, Liu J, Gong T, Su Y, Chang K and Yan P 2026 *Phys. Rev. Lett.* **136** 086703
[215] Steward C R W, Fernandes R M and Schmalian J 2023 *Phys. Rev. B* **108** 144418
[216] Luo T, Ning H, Ilyas B, von Hoegen A, Viñas Boström E, Park J, Kim J, Park J G, Juraschek D M, Rubio A and Gedik N 2025 *Nat. Commun.* **16** 6863
[217] Thingstad E, Kamra A, Brataas A and Sudbø A 2019 *Phys. Rev. Lett.* **122** 107201
[218] Kløgetvedt J N and Qaiumzadeh A 2023 *Phys. Rev. B* **108** 224424
[219] Go G, Yang H, Park J G and Kim S K 2024 *Phys. Rev. B* **109** 184435
[220] Jin Z, Yao X, Wang Z, Yuan H Y, Zeng Z, Wang W, Cao Y and Yan P 2023 *Phys. Rev. Lett.* **131** 166704
[221] Lin Z X and Zhang S 2024 *Appl. Phys. Lett.* **124** 132402
[222] Shen R C, Li J, Sun Y M, Wu W J, Zuo X, Wang Y P, Zhu S Y and You J Q 2025 *Nat. Commun.* **16** 5652
[223] Tu H T, Liao K Y, Zhang Z X, Liu X H, Zheng S Y, Yang S Z, Zhang X D, Yan H and Zhu S L 2022 *Nat. Photonics* **16** 291
[224] Sekine A, Murakami R and Doi Y 2025 *Phys. Rev. B* **112** 094413
[225] Sekine A, Murakami R and Doi Y 2026 arXiv:2509.26349
[226] Chen L, Korsch A R, Kersul C M, Benevides R, Yu Y, Alegre T P M and Gröblacher S 2026 *Nat. Commun.* **17** 1187
[227] Li J, Zhu S Y and Agarwal G S 2018 *Phys. Rev. Lett.* **121** 203601
[228] Zhang W, Xiong Y, Hu J M, Sklenar J, Subedi M M, Jungfleisch M B, Bhat V S, Li Y, Liu L, Wang Q, Luo Y K, Bae Y J and Flebus B 2026 *npj Spintronics* **4** 11